



# The Volatile Carbon-to-oxygen Ratio as a Tracer for the Formation Locations of Interstellar Comets

Darryl Z. Seligman<sup>1</sup> , Leslie A. Rogers<sup>2</sup> , Samuel H. C. Cabot<sup>3</sup> , John W. Noonan<sup>4</sup> , Theodore Kareta<sup>5</sup>, Kathleen E. Mandt<sup>6</sup> , Fred Ciesla<sup>1</sup> , Adam McKay<sup>7</sup> , Adina D. Feinstein<sup>2,11</sup> , W. Garrett Levine<sup>3</sup> , Jacob L. Bean<sup>2</sup> , Thomas Nordlander<sup>8,9</sup>, Mark R. Krumholz<sup>8,9</sup> , Megan Mansfield<sup>10</sup> , Devin J. Hoover<sup>2</sup> , and Eric Van Clepper<sup>1</sup>

<sup>1</sup> Department of the Geophysical Sciences, University of Chicago, Chicago, IL 60637, USA; [dzseligman@uchicago.edu](mailto:dzseligman@uchicago.edu)

<sup>2</sup> Department of Astronomy and Astrophysics, University of Chicago, Chicago, IL 60637, USA

<sup>3</sup> Department of Astronomy, Yale University, 52 Hillhouse, New Haven, CT 06511, USA

<sup>4</sup> Department of Physics, Auburn University, Auburn, AL, USA

<sup>5</sup> Lowell Observatory, Flagstaff, AZ, USA

<sup>6</sup> Johns Hopkins Applied Physics Laboratory, Laurel, MD, USA

<sup>7</sup> American University/NASA Goddard Space Flight Center, Greenbelt, MD, 20771, USA

<sup>8</sup> Research School of Astronomy and Astrophysics, Australian National University, Canberra, ACT 2611, Australia

<sup>9</sup> ARC Centre of Excellence for Astronomy in Three Dimensions (ASTRO-3D), Canberra, ACT 2611, Australia

<sup>10</sup> Steward Observatory, University of Arizona, 933 North Cherry Avenue, Tucson, AZ 85721, USA

Received 2022 March 28; revised 2022 May 22; accepted 2022 June 1; published 2022 July 5

## Abstract

Based on the occurrence rates implied by the discoveries of 1I/‘Oumuamua and 2I/Borisov, the forthcoming Rubin Observatory Legacy Survey of Space and Time (LSST) should detect  $\geq$  one interstellar object every year. We advocate for future measurements of the production rates of H<sub>2</sub>O, CO<sub>2</sub>, and CO in these objects to estimate their carbon-to-oxygen ratios, which trace formation locations within their original protoplanetary disks. We review similar measurements for solar system comets, which indicate formation interior to the CO snow line. By quantifying the relative processing in the interstellar medium and solar system, we estimate that production rates will not be representative of primordial compositions for the majority of interstellar comets. Preferential desorption of CO and CO<sub>2</sub> relative to H<sub>2</sub>O in the interstellar medium implies that measured C/O ratios represent lower limits on the primordial ratios. Specifically, production rate ratios of  $Q(\text{CO})/Q(\text{H}_2\text{O}) < 0.2$  and  $Q(\text{CO})/Q(\text{H}_2\text{O}) > 1$  likely indicate formation interior and exterior to the CO snow line, respectively. The high C/O ratio of 2I/Borisov implies that it formed exterior to the CO snow line. We provide an overview of the currently operational facilities capable of obtaining these measurements that will constrain the fraction of ejected comets that formed exterior to the CO snow line. This fraction will provide key insights into the efficiency of and mechanisms for cometary ejection in exoplanetary systems.

*Unified Astronomy Thesaurus concepts:* [Interstellar objects \(52\)](#)

## 1. Introduction

The composition and activity of comets and how this reflects their primordial composition, formation location, and dynamical evolution has been a long-standing subject of inquiry. In 1812, William Herschel obtained detailed observations of two comets, both of which attained different brightness levels despite similar perihelion distances (Herschel 1812a, 1812b). In order to account for this discrepancy, he speculated that the brighter comet originated from interstellar space and acquired “unperihelioned matter by moving in a parabolical direction through the immensity of space.” Laplace contemporaneously performed a surprisingly accurate estimate for the number of interstellar comets that should pass close to the Sun’s vicinity (de Laplace 1814; Heidarzadeh 2008).

The current larger census of comets can be sorted into two populations: ecliptic comets, a subset of which are Jupiter family comets (JFCs), and long-period comets (LPCs), which have isotropic distributions of inclination. It is generally

believed that the JFCs originate in the trans-Neptunian region (Leonard 1930; Edgeworth 1943, 1949; Kuiper 1951; Cameron 1962; Whipple 1964; Everhart 1972; Vaghi 1973; Delsemme 1973; Joss 1973; Fernandez 1980; Duncan et al. 1988; Quinn et al. 1990; Jewitt & Luu 1993; Prialnik et al. 2020) and migrate into the inner solar system via the Centaur region (Hahn & Bailey 1990; Levison & Duncan 1997; Tiscareno & Malhotra 2003; Di Sisto & Brunini 2007; Bailey & Malhotra 2009; Di Sisto et al. 2009; Nesvorný et al. 2017; Fernández et al. 2018; Sarid et al. 2019; Seligman et al. 2021a), while the LPCs come from the Oort cloud (Oort 1950).

While the dynamical evolution of the trajectory of a comet reveals its recent whereabouts, compositional measurements can trace the original formation location in the absence of significant postformation processing. Specifically, the ratio of combinations of molecular production rates give elemental abundance ratios. There is a precedent for using the carbon-to-oxygen (C/O) ratio as a tracer of the formation location of giant exoplanets within their protostellar disk, as this ratio should increase between the H<sub>2</sub>O, CO<sub>2</sub>, and CO freeze-out snow lines (Öberg et al. 2011). For a solar system cometary analog to these exoplanetary measurements, it was generally believed that the JFCs formed exterior to the CO snow line, while the LPCs formed between the giant planets, and that their compositions would provide evidence for this (see

<sup>11</sup> NSF Graduate Research Fellow.



Rickman 2010 and references therein for a recent review). However, space-based spectroscopic measurements of CO<sub>2</sub> and CO production rates (Ootsubo et al. 2012) revealed a surprisingly low C/O ratio in almost all solar system comets, implying formation interior to the CO snow line (A’Hearn et al. 2012). Ground-based infrared spectroscopy has demonstrated that the JFCs tend to be depleted in CO compared to the LPCs, although the sample size is small due to the difficulty of these measurements (Dello Russo et al. 2016; DiSanti et al. 2017; Roth et al. 2018; Faggi et al. 2019; Roth et al. 2020; McKay et al. 2021). A recent compositional survey of CO, CO<sub>2</sub>, and H<sub>2</sub>O for 20 cometary objects has confirmed this result (Harrington Pinto et al. 2021, 2022, in preparation). The CO activity is observed in distant Centaurs (Senay & Jewitt 1994; Crovisier et al. 1995; Womack & Stern 1997, 1999; Choi et al. 2006; Bauer et al. 2008; Gunnarsson et al. 2008; Jewitt 2009; Jaeger et al. 2011; Paganini et al. 2013; Bauer et al. 2015; Womack et al. 2017; Wierzechos et al. 2017; Schambeau 2018; James 2018; Kareta et al. 2019; Wierzechos & Womack 2020), but diminished levels of H<sub>2</sub>O activity due to low ambient temperatures prohibit accurate measurements of the volatile C/O ratio in these objects.

Given the efficacy with which the solar system ejected planetesimals via planetary migration and/or instability (Hahn & Malhotra 1999; Gomes et al. 2004; Tsiganis et al. 2005; Morbidelli et al. 2005; Levison et al. 2008; Raymond et al. 2018, 2020), it is feasible that CO-enriched comets formed exterior to the CO snow line, most of which were ejected into interstellar space. An intriguing object is C/2016 R2 (Wierzechos & Womack 2018; Cochran & McKay 2018; McKay et al. 2019), an almost hyperbolic LPC with a CO production rate  $\gtrsim 100$  that of H<sub>2</sub>O (McKay et al. 2019), suggestive that it formed exterior to the CO snow line.

The exotic composition of R2 led McKay et al. (2019) to speculate that it formed outside of our solar system. Astronomers had considered the presence of interstellar comets in the solar system prior to the detection of R2. The number density of interstellar comets was predicted based on nondetections (Sekanina 1976; McGlynn & Chapman 1989; Francis 2005; Moro-Martín et al. 2009; Engelhardt et al. 2017) with all-sky surveys such as Pan-STARRS (Jewitt 2003; Chambers et al. 2016). The forthcoming Rubin Observatory Legacy Survey of Space and Time (LSST; Jones et al. 2009; Ivezić et al. 2019), whose ability to detect transient objects has been demonstrated (Solontoi et al. 2011; Vereš & Chesley 2017a, 2017b; Jones et al. 2018), was projected to detect between 0.001 and 10 interstellar comets inferred from early estimates derived from nondetections (Cook et al. 2016).

In 2017, well before LSST’s first light, the first interstellar object, 1I/2017 U1 (‘Oumuamua), was discovered. However, observations obtained in order to measure the volatile production rates produced nondetections (Meech et al. 2017; Jewitt et al. 2017; Trilling et al. 2018). The object exhibited an extreme 6:6:1 geometry (Drahus et al. 2017; Knight et al. 2017; Belton et al. 2018; Bolin et al. 2018; Fraser et al. 2018; McNeill et al. 2018; Mashchenko 2019), a nongravitational acceleration (Micheli et al. 2018), and a moderately reddened color (Bannister et al. 2017; Masiero 2017; Ye et al. 2017; Fitzsimmons et al. 2018) consistent with its young <40 Myr age (Gaidos et al. 2017; Mamajek 2017; Almeida-Fernandes & Rocha-Pinto 2018; Feng & Jones 2018; Hallatt & Wiegert 2020; Hsieh et al. 2021).

This peculiar combination of unique physical properties led to a variety of theories regarding the provenance of ‘Oumuamua. If the nongravitational acceleration was driven by radiation pressure (Micheli et al. 2018), this would imply that ‘Oumuamua was an ultralow-density fractal aggregate (Moro-Martín 2019; Luu et al. 2020; Sekanina 2019; Flekkøy et al. 2019) or artificial millimeter thin membrane (Bialy & Loeb 2018). An artificial origin could not be confirmed, since no radio signals were found to be coming from the object (Enriquez et al. 2018; Tingay et al. 2018; Harp et al. 2019). If the acceleration was powered by outgassing (Seligman et al. 2019), the energetics could be consistent with a bulk composition of H<sub>2</sub> (Füglister & Pfenniger 2018; Seligman & Laughlin 2020; Levine & Laughlin 2021), N<sub>2</sub> (Jackson & Desch 2021; Desch & Jackson 2021), or CO (Seligman et al. 2021b). Other theories invoke a tidally fragmented planetesimal (Raymond et al. 2018; Zhang & Lin 2020) and ejection from a post-main-sequence star system (Hansen & Zuckerman 2017; Rafikov 2018a; Katz 2018) or circumbinary system (Čuk 2018; Jackson et al. 2018). However, the anomalous acceleration largely ruled out these interpretations. Grude Flekkøy & Brodin (2022) calculated observable spectral signatures that will differentiate between proposed formation theories in future objects.

A second interstellar object, 2I/Borisov, was detected in 2019. This confirmed the existence of a galactic population of interstellar objects with spatial number densities of order  $n_o \sim 1\text{--}2 \times 10^{-1} \text{ au}^{-3}$  (Trilling et al. 2017; Laughlin & Batygin 2017; Jewitt et al. 2017; Rafikov 2018b; Zwart et al. 2018; Do et al. 2018; Moro-Martín 2019, 2018; Levine et al. 2021). Object 2I exhibited a dusty coma (Jewitt & Luu 2019; Bolin et al. 2020b; Fitzsimmons et al. 2019; Ye et al. 2020; McKay et al. 2020; Guzik et al. 2020; Hui et al. 2020; Kim et al. 2020; Cremonese et al. 2020; Yang et al. 2021) with typical cometary carbon- and nitrogen-bearing species detected (Opitom et al. 2019; Kareta et al. 2020; Lin et al. 2020; Bannister et al. 2020; Xing et al. 2020; Aravind et al. 2021). It was enriched in CO relative to H<sub>2</sub>O (Bodewits et al. 2020; Cordiner et al. 2020), indicating formation exterior to the CO snow line in its original protoplanetary disk (Price et al. 2021). Lisse et al. (2022) argued that the CO enrichment could be explained if it was ejected within <20 Myr of the formation of its host system. It exhibited an outburst (Drahus et al. 2020) and fragmentation event (Jewitt et al. 2020a, 2020b; Bolin et al. 2020a; Zhang et al. 2020) due to seasonal effects (Kim et al. 2020). Its nongravitational acceleration was consistent with measured production rates (Hui et al. 2020; de la Fuente Marcos & de la Fuente Marcos 2020; Manzini et al. 2020). Curiously, atomic nickel vapor (Guzik & Drahus 2021) and abnormally high polarization (Bagnulo et al. 2021) were detected in the coma.

It is feasible that Borisov—and even possibly ‘Oumuamua, if the CO hypothesis is correct—are representative of CO-enriched comets that formed exterior to the CO snow line. Moreover, R2 may be one such comet that survived ejection from our own solar system, although its considerably higher CO/H<sub>2</sub>O ratio than that of Borisov and unexpectedly high N<sub>2</sub> abundance are difficult to explain via typical formation mechanisms (Wierzechos & Womack 2018; Mousis et al. 2022). Future detections and compositional measurements will demonstrate whether or not these objects are representative of the population. The LSST should detect  $\geq 1$  interstellar

object every year (Hoover et al. 2022), and a space-based in situ rendezvous may be performed in the upcoming decade (Seligman & Laughlin 2018; Hein et al. 2017; Meech et al. 2019; Castillo-Rogez et al. 2019; Hibberd et al. 2020; Donitz et al. 2021; Meech et al. 2021; Hibberd et al. 2022; Moore et al. 2021a). The ESA’s Comet Interceptor (Jones & ESA Comet Interceptor Team 2019; Pau Sánchez et al. 2022) mission or the NASA concept study BRIDGE (Moore et al. 2021b) may provide these observations.

In this paper, we demonstrate that the volatile C/O ratio of interstellar comets encodes their formation location with respect to the CO snow line, and we outline how this ratio can be measured with currently operational facilities. This paper is organized as follows. In Section 2, we demonstrate that the volatile C/O ratio will serve as a tracer of formation location in an interstellar comet. In Section 3, we review the measured stellar abundance ratios, as well as their systematic uncertainties and dependencies on metallicity. In Section 4, we review the measured abundances of solar system comets and establish CO<sub>2</sub>, CO, and H<sub>2</sub>O as good tracers for the C/O ratio of a comet. We show that most solar system objects with measured compositions likely formed interior to the CO snow line, while 2I/Borisov and C/2016 R2 likely formed exterior to it. In Section 5, we quantify the extent to which measurements of the coma of an interstellar comet are representative of the primordial composition based on processing in the interstellar medium (ISM) and solar system. We show that the majority of detected interstellar comets will not exhibit activity representative of their primordial compositions. Therefore, measured C/O ratios are lower limits due to the preferential desorption of CO and CO<sub>2</sub> with respect to H<sub>2</sub>O in the ISM. In Section 6, we identify C/O ratios that are definitive indications of formation exterior and interior to the CO snow line after the ISM processing. In Section 7, we outline observational facilities that can measure production rates of H<sub>2</sub>O, CO, and CO<sub>2</sub> in an interstellar comet, and we conclude in Section 8.

## 2. The C/O Ratio Traces Comet Formation Location

As presented by Öberg et al. (2011) and references therein, H<sub>2</sub>O, CO<sub>2</sub>, and CO are abundant oxygen- and carbon-bearing molecules in protoplanetary disks, which motivates consideration of carbon and oxygen as tracers of formation conditions. Importantly, these molecules condense at radii where planets are expected to form and large masses of solids are detected in protoplanetary disks (Figure 1). Observational evidence of such “snow lines” may be found based on the spatial distribution of molecular or ion tracers or through changes in the dust size distributions in the disk (Qi et al. 2013; Banzatti et al. 2015). The relative amounts of H<sub>2</sub>O, CO<sub>2</sub>, and CO in the gaseous versus solid phase will alter the C/O ratio of minor bodies. The C/O of grains, assumed to contain some refractory carbon, decreases exterior to the H<sub>2</sub>O snow line, since H<sub>2</sub>O condenses and contributes oxygen to solid materials. The ratio then rises outside of the CO<sub>2</sub> and CO snow lines due to the subsequent incorporation of these species in icy material (Figure 1). The most dramatic differences in the bulk composition and C/O ratio specifically are for objects that form interior and exterior to the CO snow line. This also defines a natural demarcation between the “outer” and “inner” regions of the system, since the CO snow line is currently located approximately at Neptune’s distance in our own solar system. It is important

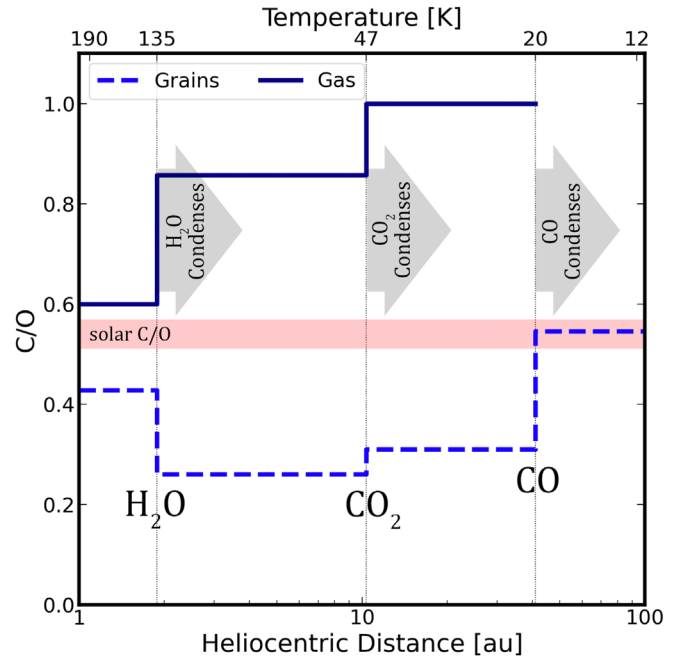


**Figure 1.** The C/O ratio of grains and gas as a function of heliocentric distance. The ratio is impacted by condensation of oxygen- and carbon-bearing molecules at and beyond their respective snow lines. The C/O profile of gas ends at the CO snow line because all major C- and O-bearing species have condensed beyond this point. Comets that form exterior to the CO snow line have higher C/O ratios than those that form interior to it. This figure is a rendition of Figure 1 in Öberg et al. (2011).

to note that the locations of these snow lines migrate as the star and disk evolve (e.g., Cieza et al. 2016).

Before focusing our attention on comets, we briefly point out the extensive precedent for using the C/O ratio to trace the formation location and evolution of extrasolar planets. Theoretical predictions indicate that carbon-rich environments can produce solids such as SiC, TiC, and graphite, as opposed to silicate-based building blocks in our own solar system (Bond et al. 2010). Similarly, carbon and oxygen are important constituents in hydrogen-dominated gas giant atmospheres (Burrows & Sharp 1999; Fortney et al. 2010; Moses et al. 2011). Whether the C/O ratio is greater or less than unity heavily influences the production of certain molecular species, including H<sub>2</sub>O, HCN, C<sub>2</sub>H, and CH<sub>4</sub> (Seager et al. 2005; Madhusudhan 2012). In turn, the C/O ratio of planetary interiors and atmospheres can be used to infer formation conditions and approximate locations within the host protoplanetary disk (Öberg et al. 2011). These considerations have been crucial for testing whether hot Jupiters ( $P < 10$  days) formed in situ or experienced inward migration. We refer the reader to Dawson & Johnson (2018) for a comprehensive review of formation theories.

The H<sub>2</sub>O, CO<sub>2</sub>, and CO abundances can also be used to trace the formation conditions of comets, which represent planetesimals that formed exterior to the H<sub>2</sub>O snow line. A’Hearn et al. (2012) attributed the scatter in production rate ratios of CO/H<sub>2</sub>O of comets to their primordial compositions, as opposed to chemical evolution from consecutive perihelion passages. They concluded that the majority of comets formed between the CO<sub>2</sub> and CO snow lines, which also explains the lower degree of scatter in CO/CO<sub>2</sub> measurements. In contrast to most of the solar system comets, 2I/Borisov’s CO/H<sub>2</sub>O was greater than unity and likely formed exterior to the CO snow



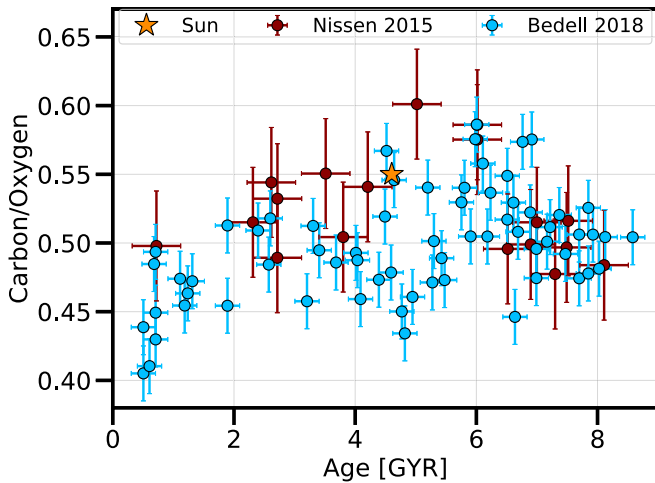


**Figure 2.** Measured C/O ratios in solar twins from Bedell et al. (2018) and Nissen (2015). The resulting combined data set has a mean C/O ratio of  $\sim 0.50$  with a standard deviation of  $\sigma \sim 0.04$ .

line in its original protoplanetary disk (Bodewits et al. 2020; Cordiner et al. 2020).

### 3. Measurements of Stellar C/O Ratios

In this section, we describe our current understanding of the C/O ratios in stars that produce interstellar comets. We discuss systematic uncertainties for measured stellar abundance ratios and the current ability to compare these measurements to cometary compositional measurements. This is essential for inferring the formation location of an interstellar comet within the protostellar disk of its host star.

#### 3.1. C/O Ratios in Solar Twins

A fundamental complication regarding measuring and comparing C/O ratios for different stars is that the stellar variations in this ratio are relatively small. Therefore, accurately comparing stellar C/O ratios requires a high level of both precision and accuracy. In stars with similar surface temperature and gravity to the Sun, commonly referred to as solar twins or solar-type stars, the C/O ratio can be measured with a high precision. The calibration to the Sun implies that the systematic errors of the abundance ratios for solar twins are almost the same for each star and mostly cancel.

Bedell et al. (2018) performed a differential study of the chemical composition of solar twins and showed that the C/O ratio in the sample did not vary significantly. However, they reported a slight dependence of this ratio on the stellar metallicity, which is a measure of heavy-element enrichment resulting from galactic chemical evolution. Nissen (2015) presented an analogous analysis for a sample of 21 solar twins and reported similar results. The reported C/O ratios for the solar twins measured by both studies are shown in Figure 2 (with data drawn from Figure 11 of Nissen 2015 and Figure 7 of Bedell et al. 2018). While the lowest-metallicity stars have lower C/O ratios, the mean C/O ratio of all of these stars is 0.50, and the standard deviation is  $\sigma = 0.04$ . All of these measurements are calibrated to measured solar abundances, which can be measured with very low uncertainties using a three-dimensional local thermodynamic equilibrium (LTE) analysis of molecular lines (Amarsi et al. 2021).

#### 3.2. C/O Ratios in All Stars

Extrapolating the C/O ratio for stars with different masses and temperatures than the Sun is less straightforward. Brewer et al. (2016) and Delgado Mena et al. (2021) performed almost-differential studies of stars that are similar but not identical to the Sun. These authors reported high precision for samples of 1617 (Brewer et al. 2016) and 1111 F, G, and K stars (Delgado Mena et al. 2021), but systematic errors in the measurements are present. Figure 5 in Delgado Mena et al. (2021) shows that the C/O ratio does vary with age, similar to what was found by Nissen (2015) and Bedell et al. (2018).

The largest source of systematic uncertainty in stellar C/O measurements is that the inferred abundance ratios are derived from spectral lines that do not form under LTE and require advanced radiative transfer calculations. Ultimately, these discrepancies vary primarily with  $T_{\text{eff}}$ ,  $\log(g)$ , and  $[\text{Fe}/\text{H}]$  (Amarsi et al. 2019). Encouragingly, the differences are small for stars where  $|T_{\text{eff}} - T_{\odot}| \leq 100$  K, so the solar twin measurements outlined in the previous subsection that do not incorporate non-LTE effects are still reliable.

An example of how these systematic errors work is shown in Figure 7 of Bedell et al. (2018), which compares their data on solar twins to the more general sample of Brewer et al. (2016). Bedell et al. (2018) demonstrated that the true C/O ratio varies slightly from star to star with an effect that is several times larger than their measurement errors; the standard deviation of the sample is  $\sim 0.04$ , while the estimated measurement uncertainties are  $\sim 0.02$ . These results are also very similar to those of the advanced non-LTE study by Amarsi et al. (2019), even though this sample included stars with a much wider range of stellar parameters.

The analysis presented by Amarsi et al. (2021) indicated that the limiting factor in measuring the solar C/O ratio is the atomic and molecular data, rather than the model solar atmosphere. Therefore, errors on the absolute abundances of carbon and oxygen do not cancel but should be combined in quadrature to calculate the uncertainty on the solar C/O ratio. The quoted accuracy is  $\sim 0.05$  dex, where  $\log(N_{\text{O}}/N_{\text{C}}) = 0.23 \pm 0.05$  dex, or  $\text{C/O} = 0.59 \pm 0.06$ . This uncertainty only applies to the absolute abundance scale. Therefore, for any homogeneous population of stars (like solar twins), the uncertainty in the scatter of the distribution is much less than 0.05 dex.

For stars that are very unlike the Sun, such as cool M-type stars, the spectra are veiled by millions of molecular lines. These introduce a different set of systematic errors that have still not been quantified and solved. Veyette et al. (2016) indicated that while the C/O ratio influences M dwarf spectra, it is unclear if synthetic spectra are good enough to fit this to a precision better than the star-to-star scatter. In case measurements of the C/O ratio in M dwarfs are acquired and calibrated on FGK stars, the 0.05 dex accuracy of the solar C/O ratio will limit those results as well. Increasing the accuracy of the atomic and molecular constants via improved laboratory measurements and theoretical calculations is the only way to reduce this dominant source of uncertainty.

#### 3.3. Assumptions for Interstellar Comet Calculations

The population of interstellar comets originates from an unknown and undifferentiated assortment of stellar populations. Therefore, in this study, we assume that the bulk

composition and mean and scatter of the elemental ratios of these stars are similar to the solar twins. Our justification for this is that there is no process that would differentially change the abundance ratios of interstellar comet-producing stars as a function of stellar mass. It is important to note that the location of the true mean has 0.05 dex uncertainty. Therefore, the predictions presented in Section 6 would scale based on the true mean when it is further constrained.

#### 4. Measurements of Cometary C/O Ratios

A classical picture of cometary formation is that the JFCs formed in the current trans-Neptunian region, while the LPCs formed between the giant planets. A’Hearn et al. (2012) presented an overview of abundance measurements in a sample of comets that had measured production rates of CO, CO<sub>2</sub>, and H<sub>2</sub>O. Based on the relatively low abundance of CO in these comets, they argued that all comets formed in the giant planet region between the CO and CO<sub>2</sub> snow lines, contrary to the classical picture. Their measurements demonstrated that JFCs formed slightly closer to the Sun than the LPCs. Recent reviews of the observed compositional properties of comets can be found in Rickman (2010), Cochran et al. (2015), Biver & Bockelée-Morvan (2016), and Bockelée-Morvan & Biver (2017).

While comets exhibit a wide variety of compositions, H<sub>2</sub>O is the primary driver of activity in the inner solar system for most of the population. The most common volatiles besides H<sub>2</sub>O are CO and CO<sub>2</sub> (Table 1 and Figure 2 in Bockelée-Morvan & Biver 2017). Typical comets consist of 0.2%–23% CO and 2.5%–30% CO<sub>2</sub> in their coma compared to H<sub>2</sub>O, where percentages are calculated by number of molecules. The CHO molecules and hydrocarbons make up, on average, ~4% and ~2%, while nitrogenous and sulfur-bearing molecules constitute ~1.5% and ~1%. The most common species in comets, on average, after CO and CO<sub>2</sub>, is CH<sub>3</sub>OH, followed by C<sub>2</sub>H<sub>6</sub>, CH<sub>4</sub>, and H<sub>2</sub>S, but these are typically at least an order of magnitude less abundant than CO<sub>2</sub> and at least factor of a few less abundant than CO. Therefore, only measuring CO, CO<sub>2</sub>, and H<sub>2</sub>O in a cometary coma can provide a reasonable first approximation of the volatile C/O ratio.

##### 4.1. Carbon and Oxygen Measured in Cometary Bodies

In this subsection, we review the currently measured compositional properties of solar system comets and calculate the inferred C/O ratios using a variety of combinations of species. As a starting place, we refer to the sample of 87 comets with measured production rates of carbon-bearing molecules C<sub>2</sub>, C<sub>3</sub>, CN, and OH over a period of 17 yr (A’Hearn et al. 1995). These comets do not have measured production rates of CO and CO<sub>2</sub>. In Figure 3, we show the C/O ratio of these comets calculated using only the production rates of C<sub>2</sub>, C<sub>3</sub>, and CN relative to H<sub>2</sub>O (inferred from OH). The conversion from OH to H<sub>2</sub>O is calculated using the branching ratio of H<sub>2</sub>O photodissociation and the heliocentric distance (Cochran & Schleicher 1993; McKay et al. 2019). These objects span a range of cometary families, and every estimated C/O ratio is <0.1, less than that expected between the H<sub>2</sub>O and CO<sub>2</sub> snow lines (Figure 1). The C/O ratio tends to increase with decreasing heliocentric distance due to the increase in C<sub>2</sub>/CN ratios, which is also reflected when plotted as a function of perihelia (see Figure 3, panel A and Figure 15 of A’Hearn et al.

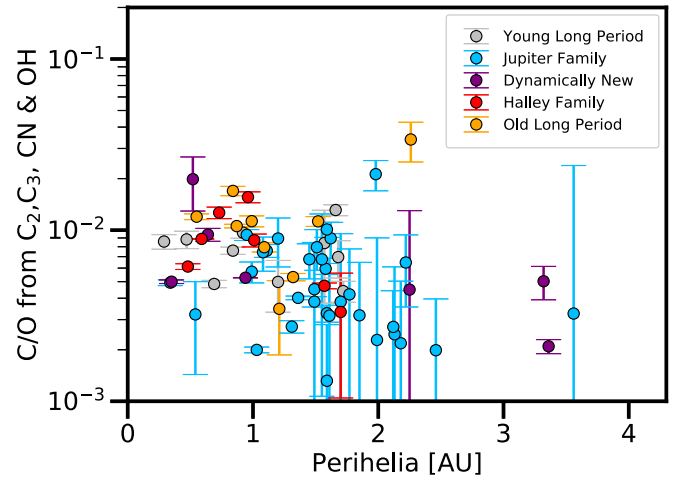


**Figure 3.** The C/O ratios for comets calculated using weighted production rates of C<sub>2</sub>, C<sub>3</sub>, CN, and H<sub>2</sub>O (from OH). These comets are in the sample presented by A’Hearn et al. (1995). The error bars are calculated by adding the reported uncertainties in quadrature scaled by the weighting of the species for the abundance ratio.

1995 and Fink 2009). This is likely related to the fact that, in addition to being released via photodissociation of more complex molecules, these species are also released from thermal degradation of carbonaceous dust grains such as the CHON grains discovered during the Halley flyby (Lawler & Brownlee 1992), a process that is more efficient closer to the Sun.

Toward constraining the C/O ratio in the volatiles of known comets, we compiled an extensive list of comets with H<sub>2</sub>O, CO, and/or CO<sub>2</sub> production rates measured at some point in their trajectory. In Table 1, we show the measured production rate ratios and associated uncertainties of CO<sub>2</sub> and CO relative to H<sub>2</sub>O in this substantially smaller sample of solar system comets. We calculate the observed C/O ratio in the coma using the equation

$$\begin{aligned} \text{C/O} = & \left[ \left( \frac{Q(\text{CO})}{Q(\text{H}_2\text{O})} \right) + \left( \frac{Q(\text{CO}_2)}{Q(\text{H}_2\text{O})} \right) + 2 \left( \frac{Q(\text{C}_2)}{Q(\text{H}_2\text{O})} \right) \right. \\ & + 3 \left( \frac{Q(\text{C}_3)}{Q(\text{H}_2\text{O})} \right) + \left( \frac{Q(\text{CN})}{Q(\text{H}_2\text{O})} \right) \\ & \left. + \left( \frac{Q(\text{CH}_3\text{OH})}{Q(\text{H}_2\text{O})} \right) \right] / \left[ 1 + \left( \frac{Q(\text{CO})}{Q(\text{H}_2\text{O})} \right) \right. \\ & \left. + 2 \left( \frac{Q(\text{CO}_2)}{Q(\text{H}_2\text{O})} \right) + \left( \frac{Q(\text{CH}_3\text{OH})}{Q(\text{H}_2\text{O})} \right) \right], \quad (1) \end{aligned}$$

where the 1 in the denominator represents the normalized H<sub>2</sub>O production rates, specifically  $Q(\text{H}_2\text{O})/Q(\text{H}_2\text{O})$ , and  $Q(X)$  is the production rate of a species in units of molecules per second. Note that OH is not included explicitly in Equation (1) because it is used to infer the H<sub>2</sub>O production rate as described previously in this section. Although O<sub>2</sub> was detected in 67P with a mean abundance of  $3.80 \pm 0.85$  relative to H<sub>2</sub>O (Bieler et al. 2015), we neglect its relative contribution to the C/O ratio in Equation (1) because this is not easily detectable remotely. We calculated the C/O ratio using only the production rates of measured species in Equation (1).

**Table 1**  
Measured Production Rate Ratios of CO<sub>2</sub> and CO with Respect to H<sub>2</sub>O, Heliocentric Distances, and Inferred C/O Ratios of Solar System Comets

Comet	Date	$r_H$ [au]	CO/H <sub>2</sub> O	(CO/H <sub>2</sub> O) <sub>err</sub>	CO <sub>2</sub> /H <sub>2</sub> O	(CO <sub>2</sub> /H <sub>2</sub> O) <sub>err</sub>	C/O	(C/O) <sub>err</sub>	Reference
1P/Halley	3/13/86	0.90	0.035	0.006	0.035	0.006			Bockelée-Morvan et al. (2004)
	3/10/86	0.86	0.065	0.006	0.059	0.005			Feldman et al. (1997)
	3/11/86	0.87	0.043	0.006	0.051	0.005			Feldman et al. (1997)
	3/16/86	0.95	0.082	0.006	0.063	0.009			Feldman et al. (1997)
	3/18/86	0.97	0.041	0.006	0.028	0.01			Feldman et al. (1997)
Mean		0.91	0.05	0.01	0.05	0.01	0.09	0.01	
153P/Ikeya-Zhang	4/13/02	0.78	0.048	0.009					CO: Disanti et al. (2002)
									H <sub>2</sub> O: dello Russo et al. (2002)
	3/20/02	0.51	0.033	0.007					CO: Biver et al. (2006)
	5/12/02	1.26	0.043	0.005					H <sub>2</sub> O: dello Russo et al. (2002)
									CO: Biver et al. (2006)
									H <sub>2</sub> O: Lecacheux et al. (2003)
Mean		0.85	0.04	0.01	0.00	0.00	0.04	0.01	
8P/Tuttle	1/27/08	1.03	0.0045	0.001					Bönnhardt et al. (2008)
Mean		1.03	0.004	0.001	0.000	0.000	0.004	0.001	
64P/Swift-Gehrels	11/23/09	2.27	<0.02		0.2905	0.017			Ootsubo et al. (2012)
Mean		2.27	0.007	0.000	0.290	0.017	0.187	0.011	
19P/Borrelly	12/30/08	2.19	<0.24		0.2410	0.009			Ootsubo et al. (2012)
Mean		2.19	0.080	0.000	0.241	0.009	0.206	0.006	
103P/Hartley 2	9/16/91	0.96			0.041				Weaver et al. (1994)
	12/31/97	1.08			0.097	0.016			Crovisier et al. (1999)
	11/4/10	0.96	0.001 50.0045		<0.2				Weaver et al. (2011)
Mean		1.00	0.003	0.000	0.068	0.016	0.063	0.014	
144P/Kushida	4/18/09	1.70	0.014	0.000 1	0.1590	0.002			Ootsubo et al. (2012)
Mean		1.70	0.014	0.0001	0.159	0.002	0.130	0.002	
67P/Churyumov-Gerasimenko	11/2/08	1.84	<0.2		0.0700	0.003			Ootsubo et al. (2012)
Mean		1.84	0.067	0.0000	0.070	0.030	0.113	0.025	
73P/S-W 3C	5/3/06	1.07	<0.0026						Dello Russo et al. (2007)
	5/27/06	0.95	0.0047	0.0019					DiSanti et al. (2007)
	5/30/06	0.95	0.0058	0.0018					DiSanti et al. (2007)
Mean		0.99	0.004	0.0019	0.000	0.000	0.004	0.002	
73P/S-W 3B	5/9/06	1.03	<0.0019						Dello Russo et al. (2007)
Mean		1.03	0.001	0.0000	0.000	0.000	0.001	0.000 5	
157P/Tritton	12/30/09	1.48	<0.14		0.0945	0.004			Ootsubo et al. (2012)
Mean		1.48	0.047	0.0000	0.095	0.004	0.114	0.003	
22P/Kopff	4/22/09	1.61	<0.03		0.2	0.02			Ootsubo et al. (2012)
	12/11/09	2.43	<0.21		0.074	0.007			Ootsubo et al. (2012)
Mean		2.02	0.040	0.0000	0.137	0.013	0.135	0.010	
81P/Wild 2	12/14/09	1.74	<0.03		0.15	0.015			Ootsubo et al. (2012)
Mean		1.74	0.010	0.0000	0.150	0.015	0.122	0.011	
88P/Howell	7/3/09	1.74	<0.06		0.25	0.02			Ootsubo et al. (2012)
Mean		1.74	0.020	0.0000	0.250	0.002	0.178	0.001	
118P/Shoemaker-Levy 4	9/8/09	2.18	<0.21		0.23	0.023			Ootsubo et al. (2012)
Mean		2.18	0.070	0.0000	0.230	0.023	0.196	0.015	

**Table 1**  
(Continued)

Comet	Date	$r_H$ [au]	CO/H <sub>2</sub> O	(CO/H <sub>2</sub> O) <sub>err</sub>	CO <sub>2</sub> /H <sub>2</sub> O	(CO <sub>2</sub> /H <sub>2</sub> O) <sub>err</sub>	C/O	(C/O) <sub>err</sub>	Reference
9P/Tempel 1	7/3/05	1.49	0.1087	0.049	0.0696	0.02			Feaga et al. (2007)
	7/5/05	1.51	0.043	0.012					Mumma et al. (2005)
	Mean	1.50	0.076	0.0305	0.070	0.020	0.120	0.030	
116P/Wild 4	5/15/09	2.22	<0.17		0.08	0.008			Ootsubo et al. (2012)
	Mean	2.22	0.057	0.0000	0.080	0.008	0.112	0.007	
C/1979 Y1 Bradfield	1/10/80	0.71	0.035	0.004	0.035	0.004			Feldman et al. (1997)
	Mean	0.71	0.035	0.0040	0.035	0.004	0.063	0.005	
C/1989 X1 Austin	5/9/90	0.83	0.017	0.008	0.021	0.008			Feldman et al. (1997)
	Mean	0.83	0.017	0.0080	0.021	0.008	0.036	0.011	
C/1990 K1 Levy	8/26/90	1.38	0.041	0.008	0.069	0.008			Feldman et al. (1997)
	9/18/90	1.13	0.084	0.015	0.133	0.015			Feldman et al. (1997)
	Mean	1.25	0.062	0.0115	0.101	0.011	0.129	0.013	
C/1995 O1 Hale-Bopp	1/21/97	1.49	0.267	0.0029					CO: DiSanti et al. (2001)
									H <sub>2</sub> O: Dello Russo et al. (2000)
	2/23/97	1.11	0.241	0.0016					CO: DiSanti et al. (2001)
									H <sub>2</sub> O: Dello Russo et al. (2000)
	3/1/97	1.06	0.271	0.0011					CO: DiSanti et al. (2001)
									H <sub>2</sub> O: Dello Russo et al. (2000)
	4/9/97	0.93	0.276	0.0022					CO: DiSanti et al. (2001)
									H <sub>2</sub> O: Dello Russo et al. (2000)
	4/16/97	0.95	0.297	0.0028					CO: DiSanti et al. (2001)
									H <sub>2</sub> O: Dello Russo et al. (2000)
	4/30/97	1.05	0.222	0.0023					CO: DiSanti et al. (2001)
									H <sub>2</sub> O: Dello Russo et al. (2000)
	5/1/97	1.06	0.280	0.0024					CO: DiSanti et al. (2001)
									H <sub>2</sub> O: Dello Russo et al. (2000)
	Mean	1.09	0.265	0.0022	0.000	0.000	0.209	0.002	
C/1996 B2 Hyakutake	3/15/96	1.24	0.149	0.033					CO: Biver et al. (1999)
									H <sub>2</sub> O: Gérard et al. (1998)
	4/1/96	0.89	0.178	0.047					CO: Biver et al. (1999)
									H <sub>2</sub> O: Gérard et al. (1998)
	4/10/96	0.67	0.328	0.02					CO: Biver et al. (1999)
									H <sub>2</sub> O: Bertaux et al. (1998)
	Mean	0.93	0.218	0.0333	0.000	0.000	0.179	0.027	
C/1999 H1 Lee	8/24/99	1.12	0.04	0.01					Biver et al. (2000)
	8/20/99	1.06	0.018	0.002					Mumma et al. (2001a)
	Mean	1.09	0.029	0.0060	0.000	0.000	0.028	0.006	
C/1999 S4 LINEAR	7/4/00	0.87	0.009	0.003					Mumma et al. (2001b)
	7/13/00	0.81	0.004	0.003					Mumma et al. (2001b)
	Mean	0.84	0.006	0.0030	0.000	0.000	0.006	0.003	
C/1999 T1 McNaught-Hartley	1/6/01	1.23	0.224	0.1					Biver et al. (2006)
	1/30/01	1.41	0.102	0.1					Biver et al. (2006)
	2/5/01	1.44	0.127	0.1					Biver et al. (2006)
	Mean	1.36	0.151	0.1000	0.000	0.000	0.131	0.087	
C/2000 WM1 LINEAR	11/23/01	1.32	0.0052	0.001					Radeva et al. (2010)
	Mean	1.32	0.005	0.0010	0.000	0.000	0.005	0.001	

Table 1  
(Continued)

Comet	Date	$r_H$ [au]	CO/H <sub>2</sub> O	(CO/H <sub>2</sub> O) <sub>err</sub>	CO <sub>2</sub> /H <sub>2</sub> O	(CO <sub>2</sub> /H <sub>2</sub> O) <sub>err</sub>	C/O	(C/O) <sub>err</sub>	Reference
C/2001 A2 LINEAR	7/10/01	1.17	0.0386	0.011					CO: Magee-Sauer et al. (2008) H <sub>2</sub> O: Gibb et al. (2007)
Mean		1.17	0.039	0.0110	0.000	0.000	0.037	0.011	
C/2002 T7 LINEAR (DN)	05/3-9/04	0.69	0.019	0.003					CO/H <sub>2</sub> O: Anderson (2010) H <sub>2</sub> O from OH: DiSanti et al. (2006)
Mean		0.69	0.019	0.0030	0.000	0.000	0.019	0.003	
C/2004 Q2 Machholz	11/29/04	1.48	0.0507	0.007					Bonev et al. (2009)
Mean		1.48	0.051	0.0070	0.000	0.000	0.048	0.007	
C/2006 OF2 Broughton	9/16/08	2.43	<0.04		0.235	0.03			Ootsubo et al. (2012)
	3/28/09	3.20	<0.26		0.58	0.06			Ootsubo et al. (2012)
Mean		2.82	0.050	0.0000	0.407	0.045	0.245	0.024	
C/2006 M4 SWAN (DN)	11/7/06	1.08	0.0049	0.0022					DiSanti et al. (2009)
	11/9/06	1.10	0.0051	0.0021					DiSanti et al. (2009)
Mean		1.09	0.005	0.0022	0.000	0.000	0.005	0.002	
C/2007 W1 Boattini (DN)	7/10/08	0.90	0.045	0.0051					Villanueva et al. (2011)
Mean		0.90	0.045	0.0051	0.000	0.000	0.043	0.005	
C/2007 N3 Lulin		1.26–1.70	0.0223	0.002	0.109 5	0.001			Ootsubo et al. (2012)
	2/1/09	1.26	0.0219	0.001					Gibb et al. (2012)
Mean		1.48	0.022	0.0015	0.110	0.001	0.106	0.001	
C/2007 Q3 Siding Spring	3/3/09	3.29	<0.1		0.19	0.07			Ootsubo et al. (2012)
Mean		3.29	0.033	0.0000	0.190	0.070	0.158	0.050	
C/2008 Q3 Garradd	7/5/09	1.81	0.26	0.03	0.28	0.03			Ootsubo et al. (2012)
	7/6/09	1.81	0.22	0.03	0.25	0.03			Ootsubo et al. (2012)
	1/3/10	2.96	<0.56		0.64	0.06			Ootsubo et al. (2012)
Mean		2.19	0.222	0.0300	0.390	0.040	0.306	0.025	
C/2009 P1 Garradd	9/18/11	2.02	0.135	0.015					Paganini et al. (2012)
	9/21/11	2.00	0.116	0.012					Paganini et al. (2012)
	9/21/11	2.01	0.046	0.011	0.116	0.009			McKay et al. (2015)
	10/10/11	1.85	0.062	0.011	0.117	0.009			McKay et al. (2015)
	1/25/12	1.62	0.147	0.032					McKay et al. (2015)
	2/27/12	1.69	0.195	0.05	0.056	0.009			McKay et al. (2015)
	3/26/12	2.00	0.63	0.32	0.085	0.02			Feaga et al. (2014)
Mean		1.88	0.190	0.0644	0.094	0.012	0.206	0.048	H <sub>2</sub> O: Bodewits et al. (2014)
29P Schwassmann-Wachmann 1	11/18/09	6.18	4.64	0.4	<0.04				Ootsubo et al. (2012)
Mean		6.18	4.640	0.4000	0.013	0.000	0.821	0.071	
C/2012 F6 Lemmon	3/31/13	0.75	0.0425	0.0064					Paganini et al. (2014)
	4/1/13	0.75	0.0382	0.0063					Paganini et al. (2014)
Mean		0.75	0.040	0.0063	0.000	0.000	0.039	0.006	
C/2012 S1 ISON (DN)	11/15/13	0.59	0.0151	0.0017					DiSanti et al. (2016)
	11/16/13	0.56	0.0091	0.0027					DiSanti et al. (2016)
	11/17/13	0.53	0.0134	0.0011					DiSanti et al. (2016)
	11/22/13	0.35	0.0181	0.0037					DiSanti et al. (2016)
Mean		0.51	0.014	0.0023	0.000	0.000	0.014	0.002	



**Table 1**  
(Continued)

Comet	Date	$r_H$ [au]	CO/H <sub>2</sub> O	(CO/H <sub>2</sub> O) <sub>err</sub>	CO <sub>2</sub> /H <sub>2</sub> O	(CO <sub>2</sub> /H <sub>2</sub> O) <sub>err</sub>	C/O	(C/O) <sub>err</sub>	Reference
C/2010 G2 Hill	1/10/12	2.5	0.91	0.23					Kawakita et al. (2014)
Mean		2.50	0.910	0.2300	0.000	0.000	0.476	0.120	
2P/Encke	11/5/03	1.19	<0.0177						Radeva et al. (2013)
Mean		1.19	0.006	0.0000	0.000	0.000	0.006	0.000	
C/2006 W3 Christensen	12/21/08	3.66	3.61	0.3	1.02	0.1			Ootsubo et al. (2012)
	6/16/09	3.13	0.98	0.06	0.42	0.06			Ootsubo et al. (2012)
Mean		3.40	2.295	0.1800	0.720	0.080	0.637	0.042	
C/2006 Q1 (McNaught)	6/3/08	2.78	<0.1		0.45	0.05			Ootsubo et al. (2012)
	2/23/09	3.64	<0.47		0.44	0.05			Ootsubo et al. (2012)
Mean		3.21	0.095	0.0000	0.445	0.050	0.272	0.025	
C/2007 G1 (LINEAR)	8/20/08	2.80	<0.17		0.23	0.02			Ootsubo et al. (2012)
Mean		2.80	0.057	0.0000	0.230	0.020	0.189	0.013	
21P/Giacobini-Zinner	10/2/98	1.25	0.1	0.06					Mumma et al. (2000)
	10/26/98	1.10	<0.032						Weaver et al. (1999)
Mean		1.18	0.055	0.0000	0.000	0.000	0.052	0.000	
C/2013 R1 Lovejoy	10/24/13	1.34	0.099	0.02					Paganini et al. (2014)
Mean		1.34	0.099	0.0200	0.000	0.000	0.090	0.018	
C/2016 R2	1/2/18	2.8	312.5	40.0	56.9	40.0			McKay et al. (2019)
Mean		2.80	312.500	40.0000	56.900	50.000	0.864	0.150	

**Note.** For comets with multiple production rate measurements, we quote the mean ratios and range of distances. We only include comets that have measured production rates of H<sub>2</sub>O, CO, and/or CO<sub>2</sub>. Reported upper limits are multiplied by a factor of 1/3 in the calculation of the C/O ratio. For multiple reported observations within 1 day of each other, we report the mean of the measurements and uncertainties. Exceptions: Nightly observations of CO and H<sub>2</sub>O were reported for comet C/2002 T7 LINEAR over a 5 day time span, for which we quote only the reported weighted average. Most of the data were drawn from Tables 1 and 2 in Dello Russo et al. (2016), Table 1 in A'Hearn et al. (2012), and Tables 1 and 3 in Ootsubo et al. (2012). For C/2016 R2, we report the mean values spanning observations through 2018 January and February, as reported by McKay et al. (2019). Updated measurements for 103P are from HST observations and the EPOXI mission flyby (A'Hearn et al. 2011).

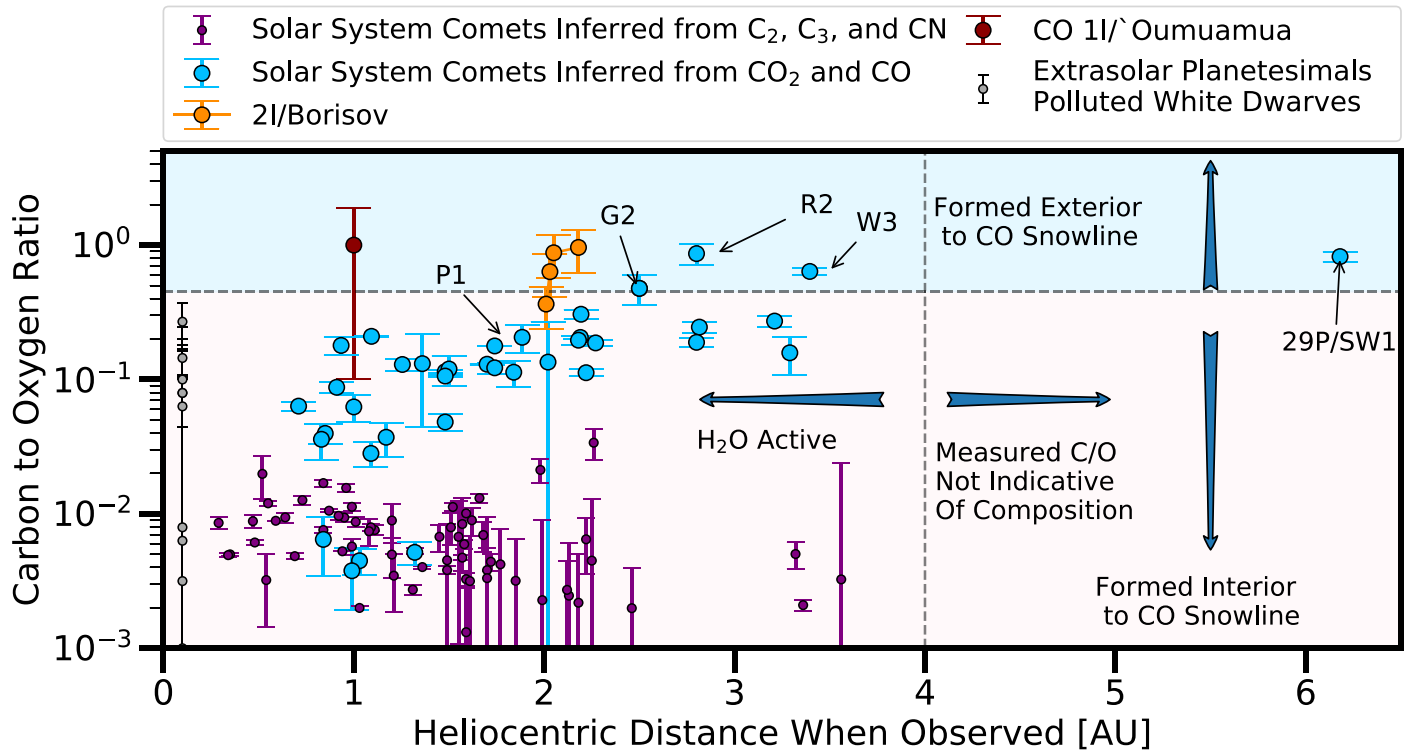


**Figure 4.** Overview of measurements of the C/O in solar system and interstellar comets. The comets presented in A’Hearn et al. (1995) with only C<sub>2</sub>, C<sub>3</sub>, CN, and OH production rates measured are shown with purple points. The comets with measured CO<sub>2</sub>, CO, and H<sub>2</sub>O production rates listed in Table 1 are shown with blue points. The C/O ratios of Borisov and ‘Oumuamua are shown in gold and red, assuming that the acceleration of ‘Oumuamua was caused by CO outgassing. We include points for all four CO detections of 2I/Borisov (see Figure 6) to highlight their relevance to this paper. The vertical dashed line indicates the region interior to which H<sub>2</sub>O is active, which explains the high inferred C/O ratio of the Centaur 29P. The blue and pink regions indicate primordial cometary C/O ratios indicative of formation interior and exterior to the CO snow line. The comets C/2009 P1 Garradd, C/2010 G2 Hill, and C/2006 W3 Christensen also have high C/O ratios and are indicated with arrows.

In Figure 4, we show the C/O ratio in the sample of comets presented in Table 1. We also include the sample of comets in Figure 3, whose C/O is generally much lower because of the lack of measured CO<sub>2</sub> and CO production rates. We also include a sample of extrasolar planetesimals from polluted white dwarfs, which reflect the bulk composition of a recently accreted planetesimal. These data include 16 polluted white dwarfs from Xu et al. (2013), Farihi et al. (2013), Xu et al. (2014), Wilson et al. (2015), and Wilson et al. (2016) (see Table 3 in Wilson et al. 2016). The polluted white dwarf events all have inferred C/O < 0.5, and all but two have C/O < 0.1.

It is important to note that the C/O derived from volatile production rates based on coma observations neglects grains that would otherwise contribute to the bulk C/O (Combi et al. 2020; Hoang et al. 2020, 2019). For example, Rubin et al. (2019) pointed out the substantial refractory inventory of carbon in the dust grains and organics of 67P/Churyumov-Gerasimenko. The oxygen inventory of dust grains also rivals that of ices (Table 4 in Rubin et al. 2019), but both depend on the dust-to-ice weight ratio, which was assumed to be around 1–3. Here we only focus on the volatile C/O, which is representative the C/O of gas and ices in the formation location of the protoplanetary disk.

There are a small subset of objects that have C/O ≥ 0.5. The most notable objects are 2I/Borisov, R2, and ‘Oumuamua. We show four postperihelion measurements of Borisov’s C/O ratio and a nominal C/O value for ‘Oumuamua, under the assumption that its nongravitational acceleration was driven by outgassing of CO (Seligman et al. 2021b). The Centaur 29P

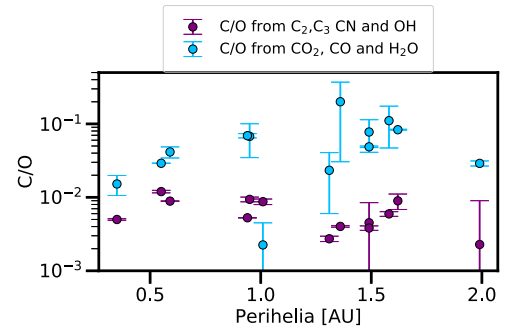


**Figure 5.** Comparison of the C/O ratio of comets inferred from production rates of CO<sub>2</sub>, CO, and H<sub>2</sub>O (blue) and C<sub>2</sub>, C<sub>3</sub>, CN, and H<sub>2</sub>O from OH (purple). These 13 comets represent the overlap between the comets in Table 1 and those presented in A’Hearn et al. (1995). With only one exception, CO<sub>2</sub> and CO are the dominant carbon-bearing species for calculating the C/O ratio.

also has a high C/O > 0.5, but its large heliocentric distance, ≥ 6 au, implies that there is likely more H<sub>2</sub>O present in the comet that is inactive. Objects R2 and 2I are atypical with respect to the bulk composition of every other cometary object that has had its production rates measured. It is worth noting that the comets C/2009 P1 Garradd, C/2010 G2 Hill, and C/2006 W3 Christensen (labeled in Figure 4) also have high C/O ratios, which may also imply a distant formation location. However, these C/O ratios are still lower than those of R2 and 2I.

In Figure 5, we show the estimated C/O ratios for comets that have measured production rates for H<sub>2</sub>O, CO, CO<sub>2</sub>, C<sub>2</sub>, C<sub>3</sub>, and CN. Consistently, with only one exception, the inferred

C/O is larger by about an order of magnitude when calculated from CO<sub>2</sub> and CO production rates compared to when calculated from C<sub>2</sub>, C<sub>3</sub>, and CN. This implies that observations of interstellar comet production rates should prioritize H<sub>2</sub>O, CO<sub>2</sub>, and CO in order to estimate the volatile C/O ratio as a tracer for formation location. However, measurements of any carbon- or oxygen-bearing species would improve the estimates of the C/O ratio. The comets in Figure 5 are 1P/Halley 1682 Q1, 8P/Tuttle 1858 A1, 19P/Borrelly 1904 Y2, 103P/Hartley 2 1986 E2, 67P/Churyumov-Gerasimenko 1969 R1, 22P/Kopff 1906 Q1, 81P/Wild 2 1978 A2, 88P/Howell 1981 Q1, 9P/Tempel 1 1867 G1, 116P/Wild 4 1990 B1, C/Bradfield 1979 Y1, C/Austin 1989 X1, and C/Levy 1990 K1.

#### 4.2. The CO-enriched Comets

In Table 2, we provide a review of all of the production rates for the various species that were measured for 2I/Borisov. In Figure 6, we show all of these production rates as function of date and heliocentric distance. While CN, C<sub>2</sub>, C<sub>3</sub>, NH<sub>2</sub>, and HCN were detected in the coma, the activity was dominated by H<sub>2</sub>O and CO. Observations sensitive to CO were only obtained after perihelion, so it is feasible that there was significant production of CO prior to perihelion.

The compositions of R2 and 2I are indicative of formation exterior to the CO snow line. In Figure 7, we show comparisons of the bulk composition of typical carbon-enriched and carbon-depleted solar system comets, R2, and 2I. The differences between these four compositions are striking, especially when viewed in a pie chart. The orders-of-magnitude higher abundance of CO ice than H<sub>2</sub>O in R2 is difficult to explain with typical cometary formation scenarios (Mousis et al. 2022).

In any case, it is feasible that planetary systems typically produce two distinct populations of comets: CO-enriched objects exterior to the CO snow line and CO-depleted objects interior to the CO snow line. The existence of a single interstellar comet with a high measured C/O ratio may imply that comets that form exterior to the CO snow line are more readily ejected, while CO-depleted objects are more likely to remain gravitationally bound to the star. The validity of this hypothesis will be revealed when more interstellar comets are detected and the fraction of the population that are CO-enriched is better constrained.

It is worth noting that cometary production rates and ratios of different species change as a function of age and position in their trajectory. Given this, we advocate for multiple observations of the relevant production rates at various heliocentric distances for future interstellar comets. We discuss this further in Sections 5, 5.4, and 7.

#### 4.3. Implications for Small Body Formation Efficiency

The host system of an interstellar comet cannot be determined from its trajectory. As we show in this subsection, however, the composition of an interstellar comet provides some constraints on the host system. We calculate the total reservoir of disk material interior and exterior to the CO ice line as a function of stellar mass in order to provide some constraints on the types of stars that can produce CO-enriched comets like Borisov.

We constructed a grid of circumstellar disk models and calculated the fraction of total material predicted to be CO-enriched. We set the inner and outer disk boundaries for each disk at 10 times the stellar radius and  $100 \text{ au} (M/M_{\odot})^{1/3}$ , respectively. In addition, we set the CO ice line at  $30 \text{ au} (M/M_{\odot})^{1/2}$ , where  $l \sim 3.5$  is the exponent in the mass–luminosity relationship  $L \propto M^l$ . The surface mass density is approximated with a power law  $\Sigma = \Sigma_0 r^{-\alpha}$ . Although the classic minimum-mass solar nebula construction adopted  $\alpha = 1.5$  (Weidenschilling 1977; Hayashi 1981), we allow for  $\alpha$  to vary.

From these values, we compute the fraction of material in the circumstellar disk that is CO-enriched and CO-depleted. We assume that the CO-enriched fraction is the percentage of mass that is located exterior to the CO ice line. Figure 8 shows the mass fraction of each disk that is CO-enriched. More massive stars push  $d_{\text{CO}}$  to farther radii and have a lower fraction of CO-enriched material. In addition, larger  $\alpha$  leads to a steeper decline in the disk surface density and also decreases the fraction of material exterior to the CO ice line.

As a point of reference, a solar-mass star would have 70%, 46%, and 15% of its disk mass exterior to the CO ice line for  $\alpha = 1.0, 1.5$ , and 2.0, respectively. A  $0.08 M_{\odot}$  M dwarf and a  $1.5 M_{\odot}$  A dwarf would have approximately 91% and 28% of their disk masses exterior to their CO ice lines for  $\alpha = 1.5$ .

While this calculation provides an estimate of the fraction of CO-enriched material as a function of stellar and disk properties, the ejection efficiencies of CO-enriched comets will depend on the cometary formation efficiency and the ejection mechanisms and rates. The propensity for stars of various masses to eject CO-enriched comets will depend on the typical outcomes of planet formation as a function of stellar mass. One possibility is that planets with a large Safronov number (the ratio of the escape velocity to the orbital velocity) form at large semimajor axes for M dwarf stars, although this idea has been theoretically disfavored (Laughlin et al. 2004). If the CO-enriched composition of Borisov is representative of typical compositions of interstellar comets, then it seems unlikely that stars larger than the Sun contribute substantially to the overall population.

### 5. The Relative Importance of Erosion in the Solar System and the ISM

A confounding mechanism that must be taken into account when predicting the molecular composition of an interstellar comet is that these objects experience processing in the ISM. The comet then experiences additional processing from stellar irradiation in the solar system. The relative importance of these two processes affects our ability to measure the primordial<sup>12</sup> composition. If the object experiences drastically more processing in the ISM than in the solar system, then the measured production rates will not be representative of the primordial composition. On the other hand, if an object experiences more processing in the solar system than in the ISM, then the measured production rates (especially postperihelion) will more directly probe the primordial composition. In this section, we quantify the relative importance of these two

<sup>12</sup> “Primordial” is loosely defined as representative of the composition upon ejection from the host system, although there is likely additional processing prior to ejection. In this paper, we do not attempt to model the pre-ejection processing due to the uncertainty in host system properties and a comet’s lifetime before ejection.

**Table 2**  
Various Production Rates for Molecules Observed for 2I/Borisov

Date	$r_H$ [au]	$Q(\text{CN})$	$Q(\text{C}_2)$	$Q(\text{C}_3)$	$Q(\text{OH})$	$Q(\text{NH}_2)$	$Q(\text{H}_2\text{O})$	$Q(\text{CO})$	$Q(\text{HCN})$	Reference
9/20/19	2.67	$3.7 \pm 0.4$	$<4$							Fitzsimmons et al. (2019)
9/20/19	2.67	$<5$	$<8$							Kareta et al. (2020)
9/27/19	2.56						$<8.2$			Xing et al. (2020)
10/1/19	2.50	$1.1 \pm 2.0$	$<2.5$							Kareta et al. (2020)
10/1/19	2.51	$1.8 \pm 0.1$	$<0.9$	$<0.3$						Opitom et al. (2019)
10/2/19	2.50	$1.9 \pm 0.1$	$<0.6$	$<0.2$	$<20$					Opitom et al. (2019)
10/9/19	2.41	$1.59 \pm 0.09$	$<0.44$							Kareta et al. (2020)
10/10/19	2.39	$1.69 \pm 0.04$	$<0.162$							Kareta et al. (2020)
10/11/19	2.38						$6.3 \pm 1.5$			McKay et al. (2020)
10/13/19	2.36	$2.1 \pm 0.1$	$<0.6$	$<0.3$	$<20$					Opitom et al. (2019)
10/18/19	2.31	$1.9 \pm 0.6$								Opitom et al. (2019)
10/20/19	2.29	$1.6 \pm 0.5$								Opitom et al. (2019)
10/26/19	2.23	$1.9 \pm 0.3$								Kareta et al. (2020)
10/31/19	2.18	$2.0 \pm 0.2$								Lin et al. (2020)
11/1/19	2.17						$7.0 \pm 1.5$			Xing et al. (2020)
11/4/19	2.15	$2.4 \pm 0.2$	$5.5 \pm 0.4$	$0.03 \pm 0.01$						Lin et al. (2020)
11/10/19	2.12	$1.9 \pm 0.5$								Bannister et al. (2020)
11/14/19	2.09	$1.8 \pm 0.2$	1.1			4.20				Bannister et al. (2020)
11/17/19	2.08	$1.9 \pm 0.5$								Bannister et al. (2020)
10/28/19–11/18/19	2.21–2.06								$<6.3$	Bergman et al. (2022)
11/25/19	2.04	$1.6 \pm 0.5$								Bannister et al. (2020)
11/26/19	2.04	$1.8 \pm 0.2$								Bannister et al. (2020)
11/26/19	2.04	$1.5 \pm 0.5$	1.1			4.80				Bannister et al. (2020)
11/30/19	2.01	$3.36 \pm 0.25$	$1.82 \pm 0.6$	$0.197 \pm 0.052$						Aravind et al. (2021)
12/1/19	2.01						$10.7 \pm 1.2$			Xing et al. (2020)
12/3/19	2.01							$3.3 \pm 0.8$		Yang et al. (2021)
12/11/19	2.01							$7.5 \pm 2.3$		Bodewits et al. (2020)
12/15-16/19	2.02							$4.4 \pm 0.7$	$0.7 \pm 0.11$	Cordiner et al. (2020)
12/19-22/19	2.03						$4.9 \pm 0.9$	$6.4 \pm 1.4$		Bodewits et al. (2020)

**Table 2**  
(Continued)

Date	$r_H$ [au]	$Q(\text{CN})$	$Q(\text{C}_2)$	$Q(\text{C}_3)$	$Q(\text{OH})$	$Q(\text{NH}_2)$	$Q(\text{H}_2\text{O})$	$Q(\text{CO})$	$Q(\text{HCN})$	Reference
12/21/19	2.03						$4.9 \pm 0.9$			Xing et al. (2020)
12/22/19	2.03	$6.68 \pm 0.27$	$2.3 \pm 0.82$	$0.714 \pm 0.074$						Aravind et al. (2021)
12/30/19	2.07							$10.7 \pm 6.4$		Bodewits et al. (2020)
1/13/20	2.16						$<5.6$	$8.7 \pm 3.1$		Bodewits et al. (2020)
1/14/20	2.17						$<6.2$			Xing et al. (2020)
2/17/20	2.54						$<2.3$			Xing et al. (2020)

**Note.** Productions rates are in units of  $10^{24}$  molecules  $\text{s}^{-1}$ , except for  $\text{H}_2\text{O}$  and  $\text{CO}$ , which are  $10^{26}$ . Errors are included where possible.



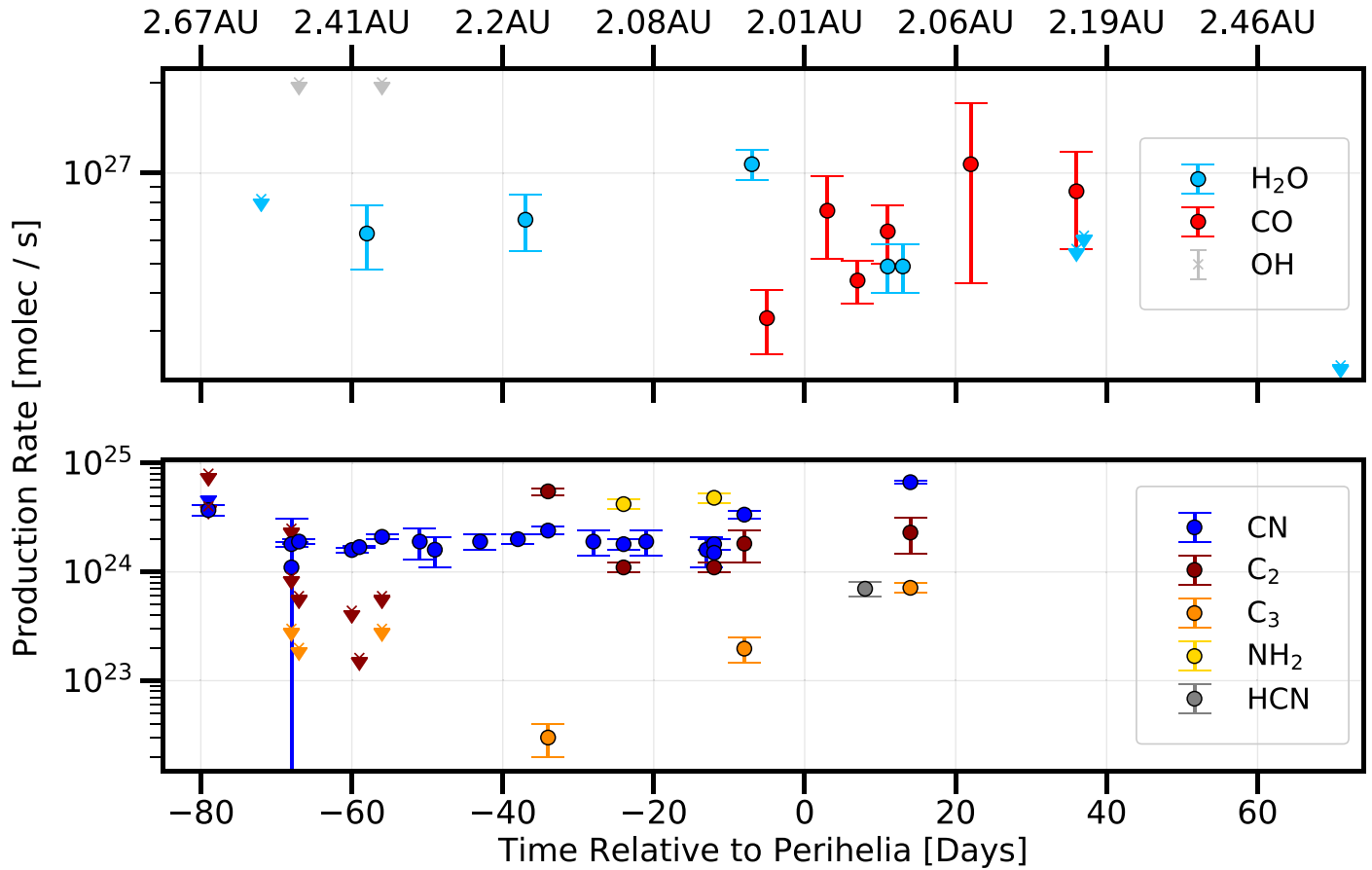


**Figure 6.** Production rate of various volatile species as a function of time relative to perihelia for the interstellar comet 2I/Borisov. The top panel shows the production rates for  $\text{H}_2\text{O}$  and  $\text{CO}$ , which are 2 orders of magnitude higher than those for  $\text{CN}$ ,  $\text{C}_2$ ,  $\text{C}_3$ ,  $\text{NH}_2$ , and  $\text{HCN}$  shown in the bottom panel. We also show upper limits measured for  $\text{OH}$  in the top panel. These production rates and their respective references are itemized in Table 2.

effects for a range of interstellar comet lifetimes and trajectories.

An interstellar comet is exposed to isotropic radiation in the ISM, primarily from cosmic rays but also from intermittent background stellar radiation. Surface volatile material will undergo nonthermal cosmic ray-induced desorption and desorption via the absorption of far-UV (FUV) photons (Hollenbach et al. 2008), which causes continuous erosion. Ice-mantled grains are transiently heated from cosmic rays and cool to their equilibrium temperature via sublimation of ice. This process was considered in Section 3 of Seligman & Laughlin (2020), Levine & Laughlin (2021), and Hoang & Loeb (2020) for an  $\text{H}_2$ -enriched ‘Oumuamua and is similar to erosion via particle bombardment (Domokos et al. 2009, 2017). The processing of interstellar objects composed of  $\text{N}_2$ ,  $\text{CO}$ ,  $\text{CO}_2$ , and  $\text{CH}_4$  due to both cosmic ray-induced desorption and collisional heating with ambient gas in the ISM was investigated by Phan et al. (2021). They estimated that a kilometer-scale progenitor could survive in the galactic cosmic-ray environment for  $\sim 1 \times 10^9$ ,  $\sim 1 \times 10^9$ ,  $\sim 2 \times 10^9$ , and  $\sim 5 \times 10^9$  yr if it was composed of  $\text{N}_2$ ,  $\text{CO}$ ,  $\text{CH}_4$ , and  $\text{CO}_2$ , respectively. These values represent upper limits, because the cosmic rays will dissociate molecules in addition to causing ices to desorb.

It is worth noting that the analysis that follows also applies to Oort cloud comets. The Oort cloud is located beyond the heliopause, with environmental conditions similar to the ISM.

### 5.1. Numerical Simulations

In this subsection, we perform numerical simulations tracking the aspect ratio, size, and density of a kilometer-scale interstellar comet like 2I/Borisov during the past 10 Gyr of evolution. We back-trace the trajectory from initial assumptions about the composition, bulk density, and size when the object enters the solar system, and we calculate the geometric changes from continuous desorption from cosmic rays and intermittent FUV photons.<sup>13</sup> The nominal solar system entrance is defined as the heliocentric distance when the change in radius becomes asymptotic.

We adopt three initial compositions for a comet composed entirely of (i)  $\text{H}_2\text{O}$ , (ii)  $\text{CO}_2$ , and (iii)  $\text{CO}$  ice with a roughly spherical nucleus with a 1 km diameter and aspect ratio of 1:1:0.98. The bulk density of the comet is assumed to be the same as that of the ice, although it is important to note that solar system comets are porous, with typical bulk densities of  $< 0.5 \text{ g cm}^{-3}$ . However, the relative mass loss of different volatiles does not sensitively depend on the assumed bulk density.

At each time step of length  $\Delta\tau$  in the simulation, we calculate the addition of an ellipsoidal shell of material desorbed from the surface. The time when the comet enters the solar system is  $t_0$ , and positive/negative  $\Delta\tau$  corresponds to

<sup>13</sup> An augmentation of the value of  $\Phi_{\text{CR}}$  could be applied to incorporate the effect of intermittent desorption via the absorption of FUV photons, but the qualitative effects of modeling both of these processes together are similar to modeling only one.

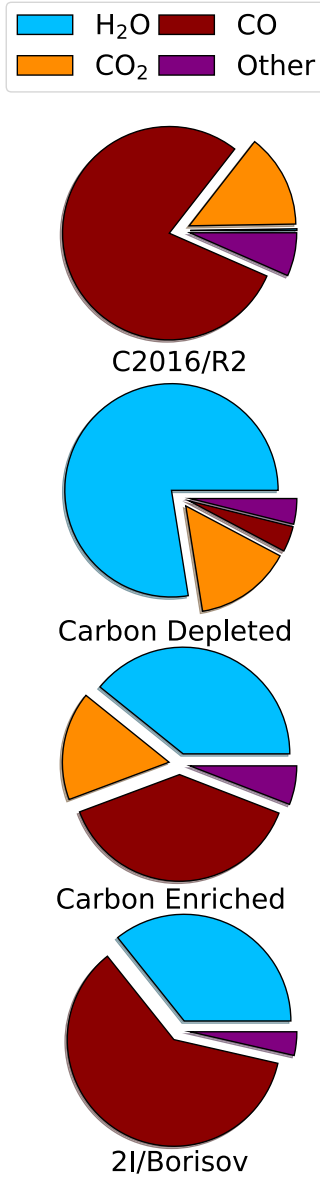


**Figure 7.** Comparison of the composition of R2, 2I, and typical carbon-enriched and carbon-depleted solar system comets. This figure is a generalized version of the analogous figure in McKay et al. (2019). It is feasible that R2 and Borisov are representative of comets that formed exterior to the CO snow line in their original protoplanetary disks, while typical solar system comets formed interior to the CO snow line. The carbon-depleted comet is representative of many of the comets in Table 1, and the carbon-enriched comet is W3 Christensen. The composition for Borisov is derived from Table 2 and references therein, and R2 is from McKay et al. (2019). The lack of CO<sub>2</sub> for 2I is only because no measurement of CO<sub>2</sub> has been reported.

time intervals moving forward/backward in time for the remainder of these calculations. The surface integrated production rate,  $\mathcal{N}$ , of sublimated molecules for a given species,  $X$  per unit time, is given by the equation

$$\mathcal{N}(t, X) = + \frac{\Sigma(t) \Phi_{\text{CR}}}{\Delta H(X)/N_A + \gamma k T_{\text{Sub}}(X)}, \quad (2)$$

where  $\Delta H(X)$  is the molar enthalpy of sublimation of the volatile species  $X$ ,  $T_{\text{Sub}}(X)$  is its sublimation temperature,  $\Sigma$  is the ellipsoidal surface area at time  $t$ , and  $\gamma$  is the adiabatic index of the escaping vapor. This calculation assumes that 100% of the energy received is deposited into desorption of ice via

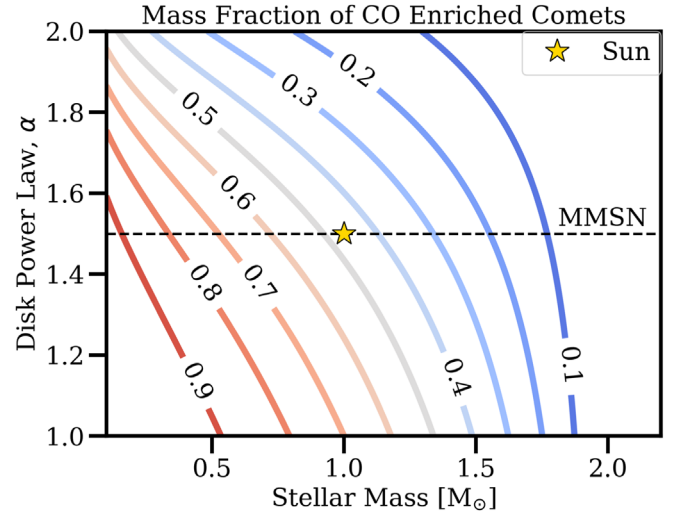


**Figure 8.** Fraction of mass located exterior to the CO ice line in circumstellar disks for a range of stellar masses and assigned surface density profiles. The dotted line indicates the classically adopted power-law exponent for the minimum-mass solar nebula.

**Table 3**  
The Enthalpy of Sublimation ( $\Delta H$ ), Solid Density ( $\rho$ ), and Temperature of Sublimation ( $T_{\text{Sub}}$ ) of Different Volatile Species

Species	$T_{\text{Sub}}$ [K]	$\rho$ [g cm <sup>-3</sup> ]	$\Delta H$ [kJ mol <sup>-1</sup> ]
CO	60	1.60	8.1
CO <sub>2</sub>	82	1.56	28.84
H <sub>2</sub> O	155	0.82	54.46

sublimation and neglects the contribution to radiative cooling of the grain via blackbody emission (which is negligible at ISM temperatures).

The change in the comet’s mass,  $\delta m$ , during each time step of length  $\Delta \tau$  is given by multiplying Equation (2) by the mass of the species and the time-step length,  $\delta m = -\mu m_u \mathcal{N} \Delta \tau$ , for a species with mass  $\mu m_u$ , where  $m_u$  is the atomic mass constant. The negative sign ensures that mass is added/removed from the body as the integration moves backward/forward in time. The resulting change in volume,  $\delta V$ , is given by  $\delta V = \delta m / \rho$ , where  $\rho$  is the bulk density of the volatile species that is sublimated. In order to explicitly demand mass conservation, we solve for roots of the cubic equation,  $\zeta(\delta h)$ , where  $\delta h$  is the change in length of each principal axis, denoted  $a$ ,  $b$ , and  $c$ ,

$$\zeta(\delta h) = \delta V - \frac{4}{3} \pi ((a + \delta h)(b + \delta h)(c + \delta h) - abc). \quad (3)$$

The signs of  $\delta V$  and  $\delta h$  depend on whether the integration is backward ( $\delta V > 0$ ,  $\delta h > 0$ ) or forward ( $\delta V < 0$ ,  $\delta h < 0$ ) in time. We verified that the results were not sensitive to the initial aspect ratios. We show the thermodynamic properties for the relevant species in Table 3.

The relative mass loss of CO and CO<sub>2</sub> with respect to H<sub>2</sub>O is shown in Figure 9. The top axis indicates the present-day maximum vertical excursion in the galactic orbit corresponding to the age on the lower  $x$ -axis. This approximates the vertical velocity dispersion, and therefore age, due to dynamical heating and primordial dispersion. ‘Oumuamua and Borisov had ages close to  $\tau_{1I} \sim 35$  Myr and  $\tau_{2I} \sim 710$  Myr, given that the maximum vertical excursion  $z_{\text{ISO}} \sim \sqrt{\tau}$  (Hsieh et al. 2021).

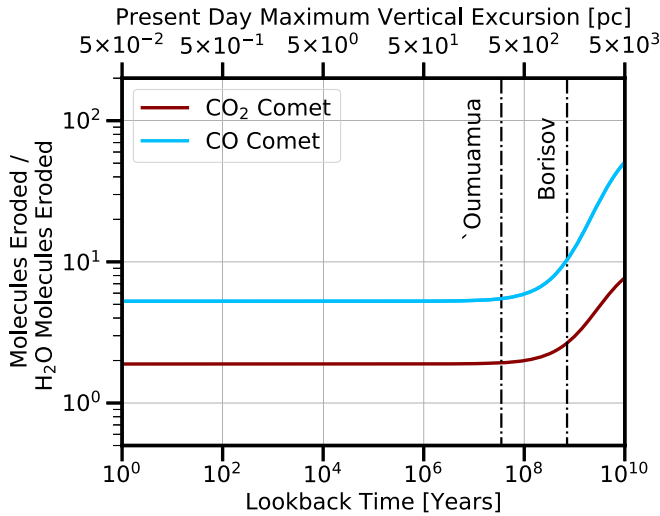


**Figure 9.** Evolution of the relative production rates of a kilometer-scale comet experiencing mass loss in the ISM. The blue and red curves indicate the time-integrated number of sublimated CO and CO<sub>2</sub> relative to H<sub>2</sub>O molecules. The lower x-axis corresponds to the look-back time prior to entering the solar system, while the upper axis shows the corresponding present-day maximum vertical excursion in the galactic orbit. The dashed-dotted lines indicate the inferred age and excursion of ‘Oumuamua and Borisov.

The H<sub>2</sub>O/CO<sub>2</sub>/CO comet grew to diameters of  $\sim 1.004/1.010/1.021$ ,  $\sim 1.400/1.963/3.078$ , and  $\sim 4.958/10.629/21.781$  km after  $10^7$ ,  $10^9$ , and  $10^{10}$  yr of (backward) evolution. The evolution is not constant after  $>10^8$  yr, when the larger surface areas of the CO<sub>2</sub> and CO comets relative to the H<sub>2</sub>O comet significantly enhance the intercepted energy flux, so these ratios should be interpreted as upper limits.

### 5.2. Analytic Approximation for ISM Processing

In this subsection, assuming a spherical geometry throughout the evolution, we derive a simplified analytic form for the evolution in the ISM as a function of age. At any time step in the integration, the rate of change of the comet’s volume due to the ongoing ablation is given by

$$\frac{dV(t, X)}{dt} = -3 \left( \frac{4\pi}{3} \right)^{1/3} \left( \frac{\mu m_u}{\rho} \right) \times \left( \frac{\Phi_{CR}}{\Delta H(X)/N_A + \gamma k T_{Sub}(X)} \right) V(t)^{2/3}, \quad (4)$$

where  $V(t)$  is the volume of the comet at time  $t$  in the integration. The assumption of spherical symmetry allows for the substitution for surface area  $\Sigma = 3V/R = 3(4\pi/3)^{1/3}V^{2/3}$ , where  $R$  is the radius of the comet. Equation (4) can be integrated via the expression

$$\int_{V_0}^{V_i} V^{-2/3} dV = - \int_{t_0}^{t_0 - \tau_{ISO}} 3 \left( \frac{4\pi}{3} \right)^{1/3} \left( \frac{\mu m_u}{\rho} \right) \times \left( \frac{\Phi_{CR}}{\Delta H/N_A + \gamma k T_{Sub}} \right) dt, \quad (5)$$

where  $V_0$  represents the volume when it enters the solar system, while  $V_i$  is the volume at the time of ejection. Here  $\tau_{ISO}$  is the duration of the journey in the ISM or ISO age and is positive. Equation (5) can be integrated to give the linear function for the

radius,

$$R_i = R_0 + \left( \frac{\mu m_u}{\rho} \right) \left( \frac{\Phi_{CR}}{\Delta H/N_A + \gamma k T_{Sub}} \right) \tau_{ISO}, \quad (6)$$

where  $R_0$  and  $R_i$  are the radius when it enters the solar system and upon ejection, respectively.

We verified that Equation (6) produced good agreement with the numerical calculations shown in Figure 9 in the previous subsection. Equation (6) can be generalized for any mixture of volatiles as long as the bulk density of the comet remains constant. After this processing transpires, the outer rind of a comet with a mixture of ices will be devoid of the molecules with the lowest  $\Delta H$  and  $T_{Sub}$ . The interior of the comet will still retain the composition upon ejection.

### 5.3. Solar System Processing

In this subsection, we extend the previous calculation to account for processing in the solar system. Since the interior composition remains intact in the ISM, postperihelion observations will be representative of the primordial compositions if the solar system processing removes the ISM-processed surface.

To quantify this effect, we derive an analytic function for the radius evolution in the solar system, analogous to Equation (6) for the ISM. A schematic diagram of these two processes is shown in Figure 10. For the encounter in the solar system, the rate of change of the comet’s volume is

$$\frac{dV(t, X)}{dt} = -3 \left( \frac{4\pi}{3} \right)^{1/3} \left( \frac{1}{(\Delta H/N_A + \gamma k T_{Sub})} \right) \times \left( \frac{\mu m_u}{\rho} \right) \left( \frac{L_{\odot}}{4\pi r_H^2} \right) \xi (1 - p) V(t)^{2/3}, \quad (7)$$

where  $L_{\odot}$  is the solar luminosity,  $\xi$  is the ratio of the projected surface area to the total surface area,  $p$  is the Bond albedo,  $r_H$  is the heliocentric distance at a given point in the trajectory, and  $\xi = 1/4$  averaged over all projection angles (Meltzer 1949). This value is an upper limit because we do not include radiative cooling, which would decrease the magnitude of the mass lost in the solar system.<sup>14</sup>

From the conservation of angular momentum, we have  $r_H^2 \dot{\theta} = b v_{\infty}$ , where  $\theta$  is the angle from the perihelia in the plane of the hyperbolic trajectory,  $v_{\infty}$  is the hyperbolic excess velocity, and  $b$  is the impact parameter. Combining  $\dot{\theta} = b v_{\infty} / r_H^2$  with Equation (7) to change the integration variables from  $t$  to  $\theta$  leads the  $r_H^2$  factors to conveniently cancel and yields

$$\int_{V_0}^{V_f} V^{-2/3} dV = - \int_{\theta_{min}}^{\theta_{max}} 3 \left( \frac{4\pi}{3} \right)^{1/3} \left( \frac{\mu m_u}{\rho} \right) \left( \frac{1}{b v_{\infty}} \right) \times \left( \frac{1}{(\Delta H(X)/N_A + \gamma k T_{Sub}(X))} \right) \times \left( \frac{L_{\odot}}{4\pi} \right) (\xi (1 - p)) d\theta, \quad (8)$$

where  $V_f$  is the final volume after the solar system encounter. The angle between the asymptotes for a hyperbolic orbit is

<sup>14</sup> The reradiation efficiency for ‘Oumuamua was calculated in Figure 1 of Seligman & Laughlin (2018) and did reach close to 100% for a short time span surrounding perihelion.

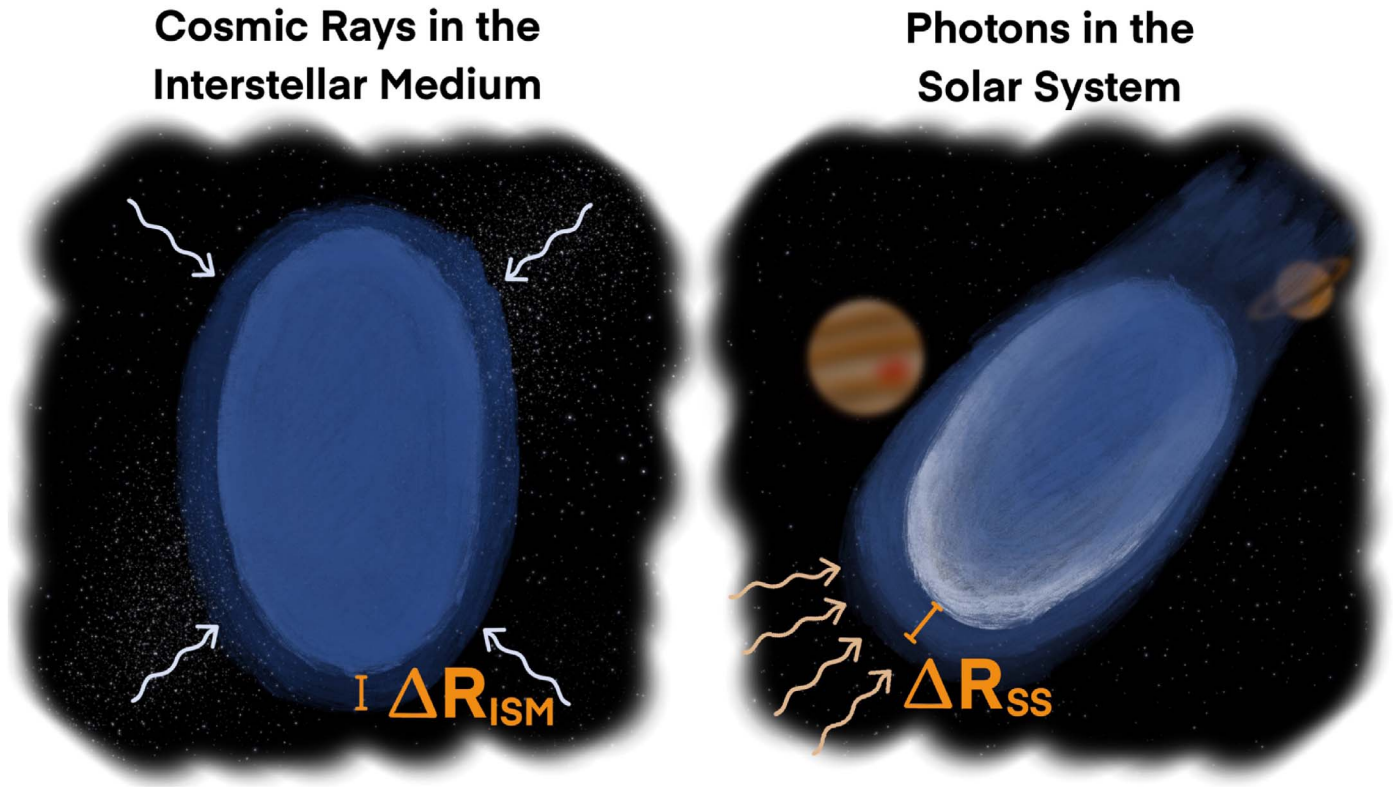


**Figure 10.** Schematic diagram showing two distinct stages of an interstellar comet's lifetime. On the left-hand side, the comet is traveling through the ISM. It experiences continuous isotropic radiation and interaction with ambient gas, which removes volatile material off of the surface. The overall reduction of the radius in this phase of the object's lifetime is denoted as  $\Delta R_{\text{ISM}}$ . On the right-hand side, the comet has finished its journey through the ISM and is traveling through the solar system. There is a focused ablation of material due to sublimation from solar irradiation, which produces a cometary tail. Averaged over many tumbles of the object and orientations to the Sun, this erosion produces an additional change in radius, which we denote as  $\Delta R_{\text{SS}}$ .

given by<sup>15</sup>

$$\theta_{\text{max}} - \theta_{\text{min}} = 2 \cos^{-1}(-1/e), \quad (9)$$

where the eccentricity of the trajectory is in turn related to  $b$  and  $v_{\infty}$ ,

$$e^2 = 1 + \frac{b^2 v_{\infty}^4}{G^2 M_{\odot}^2}. \quad (10)$$

Equation (8) integrates to

$$R_f = R_0 - 2 \left( \frac{\mu m_u}{\rho} \right) \left( \frac{1}{\Delta H / N_A + \gamma k T_{\text{Sub}}} \right) \times \left( \frac{L_{\odot}}{4\pi} \right) (\xi(1-p)) \left( \frac{1}{b v_{\infty}} \right) \left( \cos^{-1} \left( -\frac{1}{e} \right) \right), \quad (11)$$

where  $R_f$  is the final radius of the object after the encounter with the solar system.

#### 5.4. The Relative Importance of Processing in the ISM and the Solar System

In the previous two subsections, we calculated the change in radius of an interstellar comet due to (i) nonthermal cosmic ray-induced desorption in the ISM (Equation (6)) and (ii) stellar irradiation during the encounter with the solar system (Equation (11)). In this subsection, we evaluate the relative

importance of these two processes as a function of the age and trajectory of an interstellar comet. We define the change in radius in the ISM and solar system as  $\Delta R_{\text{ISM}} = R_i - R_0$  and  $\Delta R_{\text{SS}} = R_0 - R_f$ . The relative change in radius is given by the dimensionless quantity,

$$\frac{\Delta R_{\text{SS}}}{\Delta R_{\text{ISM}}} = \frac{\cos^{-1}(-1/e)}{2\pi} \left( \frac{L_{\odot} \xi(1-p)}{\Phi_{\text{CR}} b v_{\infty} \tau_{\text{ISO}}} \right). \quad (12)$$

Compositional measurements will be representative of the primordial material for objects where  $\Delta R_{\text{SS}}/\Delta R_{\text{ISM}} \geq 1$ . Equation (12) can be written as the following scaled relationship:

$$\frac{\Delta R_{\text{SS}}}{\Delta R_{\text{ISM}}} = 0.59 \left( \frac{1-p}{0.9} \right) \left( \frac{0.85 \text{ au}}{b} \right) \left( \frac{26 \text{ km s}^{-1}}{v_{\infty}} \right) \times \left( \frac{\cos^{-1}(-1/e)}{\cos^{-1}(-1/1.2)} \right) \left( \frac{3.5 \times 10^8 \text{ yr}}{\tau_{\text{ISO}}} \right), \quad (13)$$

where the values of  $b$ ,  $v_{\infty}$ ,  $e$ , and  $\tau_{\text{ISO}}$  of 'Oumuamua have been used.

We show the relative change in radius in the solar system and ISM for a range of  $b$  and  $v_{\infty}$  in Figure 11 for Borisov- and 'Oumuamua-aged objects. 'Oumuamua experienced comparable erosion in the solar system and ISM with  $\Delta R_{\text{SS}}/\Delta R_{\text{ISM}} = 0.59$ , while Borisov had  $\Delta R_{\text{SS}}/\Delta R_{\text{ISM}} < 10^{-2}$ . Previously, Kim et al. (2020) estimated that Borisov only lost  $\sim 0.4$  m of surface material in the solar system and similarly concluded that compositional observations were not representative of the primordial material. Hoover et al. (2022) presented the orbital

<sup>15</sup> The inverse cosine function in Equation (9) is restricted to the principal branch such that  $\theta_{\text{max}} - \theta_{\text{min}}$  ranges between  $\pi$  and  $2\pi$ .



distribution of interstellar objects detected by LSST, assuming that all of the objects had an absolute magnitude similar to that of 'Oumuamua. We show the cumulative distribution functions for  $b$  and  $v_\infty$  in Figure 12, from Figures 12 and 15 of Hoover et al. (2022). The LSST will detect objects out to  $b \sim 3$  au with  $20 \text{ km s}^{-1} < v_\infty < 60 \text{ km s}^{-1}$ . These limits are reflected in Figure 11. Roughly 80% of the detected objects will have  $v_\infty < 40 \text{ km s}^{-1}$  and  $b < 2$  au. Objects the age of 'Oumuamua will have  $\Delta R_{\text{SS}}/\Delta R_{\text{ISM}} \sim 1$  only for  $b \leq 0.5$  au. No objects the age of Borisov will have  $\Delta R_{\text{SS}}/\Delta R_{\text{ISM}} \geq 1$ . From incorporating the results of the marginal cumulative distribution functions, we calculate that  $<5\%$  of objects with ages similar to 'Oumuamua will have  $\Delta R_{\text{SS}}/\Delta R_{\text{ISM}} > 1$ . Spectroscopic measurements during a tidal disruption event, activity-driven disintegration event, or space-based impactor collision could reveal the primordial composition.

### 5.5. Estimating Primordial Composition from Observed Production Rates

In this subsection, we outline a method to approximate the primordial C/O ratio from the observed production rates. As we showed in the previous subsection, the majority of interstellar comets will not exhibit activity representative of their primordial composition (unless they break apart under the action of tides, activity, rotation, and/or collisions). Moreover, processing in the ISM should preferentially remove CO and CO<sub>2</sub> with respect to H<sub>2</sub>O (Figure 9). Therefore, the C/O ratio inferred from H<sub>2</sub>O, CO<sub>2</sub>, and CO production rates after processing are lower limits on the primordial C/O ratio.

The volatile C/O ratio of an interstellar comet that has production rates for CO<sub>2</sub>, CO, and H<sub>2</sub>O measured during its apparition is given by

$$(C/O)_{\text{Obs}} = \left[ \left( \frac{Q(\text{CO})}{Q(\text{H}_2\text{O})} \right)_{\text{Obs}} + \left( \frac{Q(\text{CO}_2)}{Q(\text{H}_2\text{O})} \right)_{\text{Obs}} \right] / \left[ 1 + \left( \frac{Q(\text{CO})}{Q(\text{H}_2\text{O})} \right)_{\text{Obs}} + 2 \left( \frac{Q(\text{CO}_2)}{Q(\text{H}_2\text{O})} \right)_{\text{Obs}} \right], \quad (14)$$

where the subscript "Obs" indicates the quantity when observed in the solar system. This is analogous to the observed C/O ratio in Equation (1).

The goal of this subsection is to derive an approximate upper limit on the primordial C/O ratio from the observed ratio. In order to estimate this limit, we assume that the time-averaged desorption of molecules in the ISM affects all species equally (i.e., each species has a similar cross section to galactic cosmic rays). The ratio of production rates in the ISM likely varies at any given snapshot during this journey. However, we assume that the total time-averaged ratio of molecules desorbed is mediated by the thermodynamic properties of each species. As long as the comet is old enough such that this time averaging is a reasonable approximation, then the ratio of molecules desorbed is independent of the comet's age. In this idealized scenario, the composition of the processed comet surface reaches a steady state (depleted in the more volatile species) wherein the relative ablation rates of the various species are balanced by the addition of fresh unprocessed primordial material at the base of the active volume as the processed surface extends deeper into the body due to the ongoing erosion.

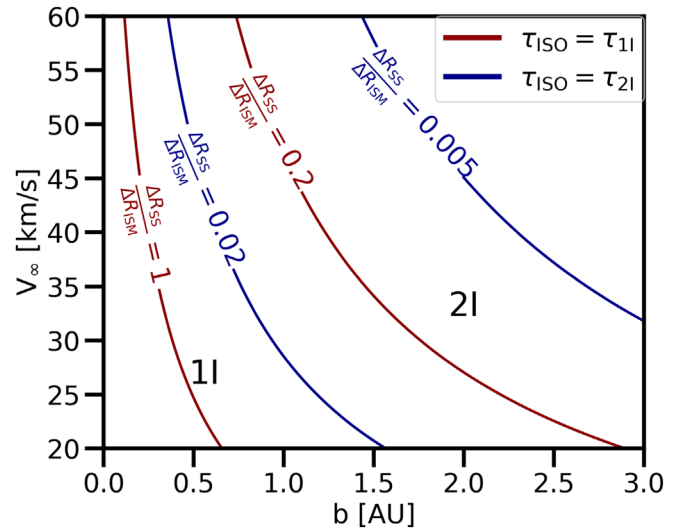


**Figure 11.** Relative erosion of an interstellar comet in the solar system and ISM. We show the change in radius of the comet in the solar system divided by the change in radius in the ISM, calculated for a range of impact parameters and hyperbolic velocities using Equation (13). The ratio for objects the age of 11/'Oumuamua and 21/Borisov are shown in red and blue contours. The locations of these two detected interstellar objects are indicated.

The steady-state composition of the processed surface is set by the thermodynamic properties of the species and the initial primordial composition of the comet. Assuming that the observed C/O ratio of the coma during its apparition in the solar system represents the composition of the ISM-processed surface of the nucleus,

$$\left( \frac{Q(X)}{Q(\text{H}_2\text{O})} \right)_{\text{Obs}} = \frac{1}{\Phi_X} \left( \frac{Q(X)}{Q(\text{H}_2\text{O})} \right)_{\text{Prim}}, \quad (15)$$

where the ratio  $\Phi_X$  is defined as

$$\Phi_X = \left( \frac{\Delta H(\text{H}_2\text{O})/N_A + \gamma k T_{\text{Sub}}(\text{H}_2\text{O})}{\Delta H(X)/N_A + \gamma k T_{\text{Sub}}(X)} \right). \quad (16)$$

In the case where the production rates of CO<sub>2</sub>, CO, and H<sub>2</sub>O are measured, the primordial C/O ratio can be estimated as

$$(C/O)_{\text{Prim}} = \left[ \Phi_{\text{CO}} \left( \frac{Q(\text{CO})}{Q(\text{H}_2\text{O})} \right)_{\text{Obs}} + \Phi_{\text{CO}_2} \left( \frac{Q(\text{CO}_2)}{Q(\text{H}_2\text{O})} \right)_{\text{Obs}} \right] / \left[ 1 + \Phi_{\text{CO}} \left( \frac{Q(\text{CO})}{Q(\text{H}_2\text{O})} \right)_{\text{Obs}} + 2 \Phi_{\text{CO}_2} \left( \frac{Q(\text{CO}_2)}{Q(\text{H}_2\text{O})} \right)_{\text{Obs}} \right]. \quad (17)$$

The values of  $\Phi_{\text{CO}_2} = 1.89$  and  $\Phi_{\text{CO}} = 6.41$  are calculated using Equation (16) and the values in Table 3. Since  $\Phi_{\text{CO}_2}, \Phi_{\text{CO}} > 1$ , the measured C/O ratios of interstellar comets based on CO<sub>2</sub>, CO, and H<sub>2</sub>O production rates measured in the solar system are lower limits on the interstellar comets' primordial C/O ratios.

In Figure 13, we show the ratio of the primordial to observed C/O ratios given by Equations (14) and (17) for a range of production rates of CO and CO<sub>2</sub> relative to H<sub>2</sub>O. This transformation can be applied to the production rates of interstellar comets to estimate their primordial C/O values and can be extended to include measured production rates for any species. For Borisov, the production rates of CO and H<sub>2</sub>O



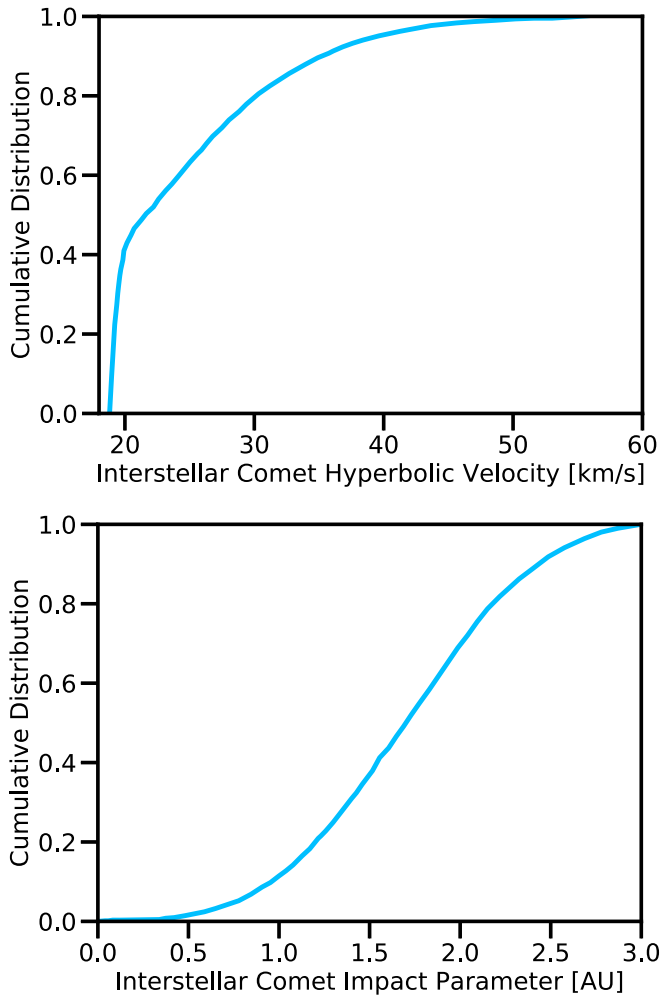


**Figure 12.** Cumulative distribution functions for impact parameter and hyperbolic excess velocity for interstellar objects that will be detected by the LSST from Figures 12 and 15 in Hoover et al. (2022). These are calculated using a detailed population synthesis assuming that the interstellar objects were as bright as ‘Oumuamua.

measured between 2019 December 19 and 22 imply a C/O ratio of  $\sim 0.56$ , which would correspond to a primordial C/O ratio of  $\sim 0.89$ .

Admittedly, the assumptions involved in transforming from the observed to primordial C/O ratio (Figure 13) are highly idealized. The processing in the ISM of an interstellar comet is likely a much more complicated process than the one described here. Therefore, we only apply the transformation derived here to estimate limits on the primordial composition in Section 6. The purpose of this calculation is not to calculate a definitive primordial C/O ratio from the observed one. Interior compositional measurements obtained during an interception mission would provide a more accurate calibration of the transformation from observed to primordial compositional ratios.

### 5.6. Protective Shielding in the ISM

Borisov was enriched in CO compared to most solar system comets, despite the fact that it had  $\Delta R_{SS}/\Delta R_{ISM} \ll 1$ . Moreover, if the nongravitational acceleration of ‘Oumuamua was caused by the sublimation of CO (Seligman et al. 2021b), then the C/O ratio would have been close to unity. Therefore, it

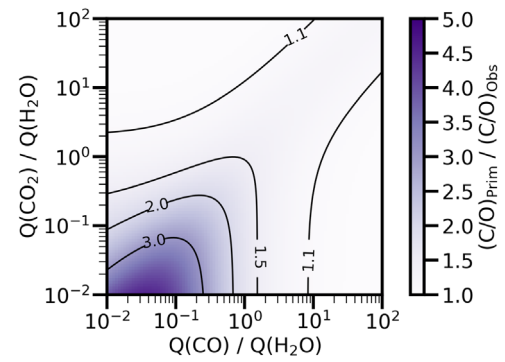


**Figure 13.** Transformation from the observed to primordial C/O ratio of an interstellar comet. The ratio is calculated by evaluating Equations (14) and (17) for a range of production rate ratios. Processing decreases the observed C/O ratio due to preferential desorption of CO and CO<sub>2</sub> relative to H<sub>2</sub>O.

may be that the preferential erosion of CO in an interstellar comet is a minor effect.

It is possible that the exposure to the galactic radiation environment produces a comet-like object with an insulating crust of volatile-depleted ‘regolith’ of low thermal conductivity (Cooper et al. 2003). This regolith could shield subsurface layers, leaving them intact. This was initially pointed out as a possible explanation for ‘Oumuamua’s lack of coma by Jewitt et al. (2017) and elaborated upon with detailed thermal modeling by Fitzsimmons et al. (2018). Seligman & Laughlin (2018) demonstrated that less than 10 cm of regolith coating was sufficient to protect subsurface volatiles from sublimating, even when exposed to the solar radiation (Figure 1 in that paper). This layer is smaller than the layer removed from Borisov during its solar system passage estimated by Kim et al. (2020). Such mantled regolith crusts could help to preserve the interior of an interstellar comet through interstellar space.

## 6. Inferring the Formation Location of Future Interstellar Comets

In this section, we investigate the feasibility of inferring the formation location of an interstellar comet relative to the CO snow line in its host protostellar disk. Assuming that interstellar comet host stars have C/O ratios of  $\sim 0.5$  (Section 3), a primordial composition with C/O  $> 0.5$  implies formation exterior to the CO snow line.

As we showed in the previous section, processing increases the C/O ratio of an interstellar comet. However, mechanisms such as (i) self-shielding (Section 5.6), (ii) inefficient desorption, and (iii) sputtering could decrease the efficiency of this effect. Therefore, measured C/O ratios can be interpreted as a lower limit on the primordial ratio. In Figure 14, we show the observed C/O ratio of an interstellar comet for a range of measured production rate ratios. In the overplotted contours, we show the regions where the observed and primordial C/O ratios are equal to 0.5 based on the transformations from processing. A measured C/O ratio  $> 0.5$  is definitive evidence that the interstellar comet formed exterior to the CO snow line in its host system. If the measured observed C/O ratio is  $< 0.5$ , but the primordial C/O ratio is  $> 0.5$ , it is still possible that the comet formed exterior to the CO snow line and experienced preferential desorption of CO during processing. If the measured C/O ratio is  $\leq 0.2$ , then the object definitively formed interior to the CO snow line.

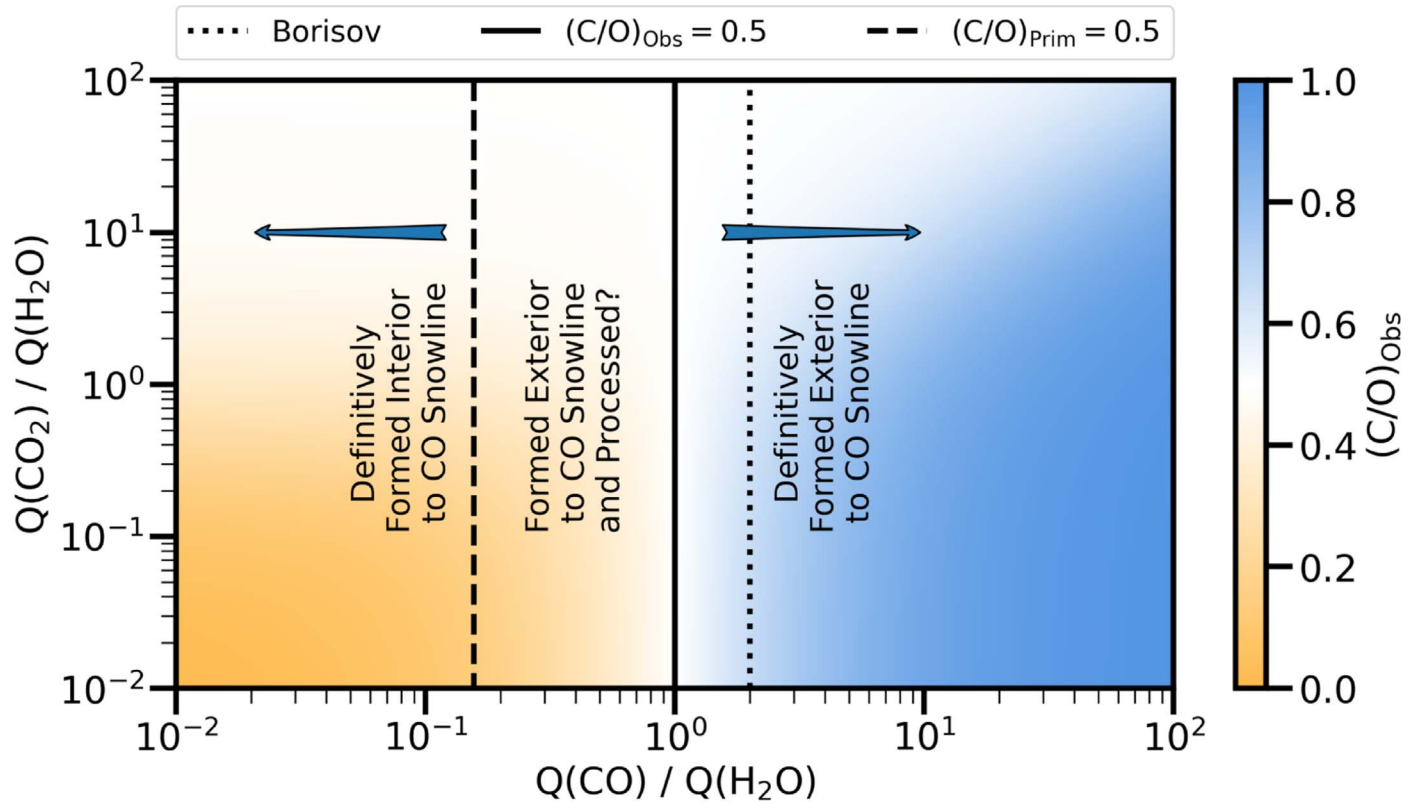


**Figure 14.** Observed C/O ratio of an interstellar comet as a function of the measured production rates of CO and CO<sub>2</sub> relative to H<sub>2</sub>O. The solid line indicates the region where the observed C/O ratio is 0.5. Since processing preferentially removes CO and CO<sub>2</sub> relative to H<sub>2</sub>O, comets to the right of this line formed exterior to the CO snow line. The dashed line indicates where the primordial C/O ratio is 0.5, using the transformation presented in Figure 13. Objects to the left of this line formed interior to the CO snow line. Objects in between both of these lines could have formed exterior to the CO snow line with primordial C/O ratios greater than 0.5, with their observed C/O ratios altered due to processing. The location of Borisov is indicated with a dotted line, implying that it formed exterior to the CO snow line.

In Figure 14, we indicate the measured C/O ratio of Borisov safely within the region that implies definitive formation exterior to the CO snow line. Future detections of interstellar comets and measurements of the production rates of CO<sub>2</sub>, CO, and H<sub>2</sub>O will constrain the fraction of the population that formed exterior to the CO snow line.

## 7. Observational Capability and Planning

### 7.1. Observatories and Science Objectives

In this section, we describe observations of an interstellar comet that would reveal its formation location and the facilities capable of obtaining them. We identify the primary science goal as constraining the elemental C/O ratio in the gaseous coma of the interstellar comet and describe several other secondary objectives. The following quantities and ratios would be useful to measure for this goal.

1. Elemental ratios (C/O, N/O, S/O) (direct from UV, inferred from VIS/NIR/submillimeter molecule abundances)
2. Molecular abundances (NUV/VIS/NIR/submillimeter)
  - (a) Molecules: H<sub>2</sub>O, CO, CO<sub>2</sub> (N/UV, VIS, NIR, submillimeter)
  - (b) Radicals: OH, CN, C<sub>2</sub>, C<sub>3</sub> (NUV, VIS, NIR)

Production ratios of “parent” volatiles like H<sub>2</sub>O, CO<sub>2</sub>, or CO at regular intervals during the apparition will provide a direct measurement of the C/O ratio. Large field-of-view observations of the broader atomic comae in the ultraviolet with

fortuitous viewing geometry would provide atomic carbon and oxygen abundances. Regular observations of daughter molecules (produced via the breakdown of “parent” molecules) such as OH, CN, and C<sub>2</sub> would offer an additional constraint on the bulk carbon-compound abundance. Measured daughter molecules would also enable comparisons with solar system comets that do not have measured CO<sub>2</sub>, CO, and H<sub>2</sub>O production rates.

### 7.2. Facilities and Approaches

In this subsection, we identify observational facilities capable of achieving the identified science goals. For many of the goals, there are only a handful of ground- or space-based facilities capable of achieving them. A nonexhaustive comparison of the objectives, required wavelength coverage, and relevant facilities are listed in Table 4.

In general, measuring the C/O ratio directly requires a census of all relevant ions, atoms, molecules, and radicals in the coma. However, a decent understanding can be achieved through monitoring the production rates of H<sub>2</sub>O, CO, and CO<sub>2</sub> (Figure 3). Measuring the production rates of these species directly will require Hubble or the James Webb Space Telescope (JWST) and a ground-based millimeter-wave facility such as the Atacama Large Millimeter/submillimeter Array (ALMA). The CO is observable from the ground at millimeter wavelengths and in the near-infrared (NIR), while H<sub>2</sub>O and CO<sub>2</sub> require space-based infrared observations in most cases. With the Spitzer satellite past its lifetime, JWST is the most capable space-based facility sensitive to these infrared emissions. If the comet is sufficiently bright, H<sub>2</sub>O and CO can be

**Table 4**

Science Goals, the Observatories Capable of Making the Relevant Observations, and Limiting Factors to Support Comprehensive Characterization of the Next Interstellar Object

Science Goal	Wavelength Relevant	Regime Observatories	Limitations
Atomic abundances (direct)	900–2100 Å	HST (STIS, COS)	Small FOV, operational lifetime
	3000–5000 Å	VLT (UVES)	
	4200–11000 Å	Keck (HIRES)	
	1216 Å	SOHO (SWAN)	Pointing, limited to hydrogen
Relative atomic abundances (inferred from daughter products)	3200–10000 Å	Keck	
	3000–25000 Å	VLT (XSHOOTER)	
	3200–10000 Å	LBT	Monsoon season dead time
Molecular abundance (H <sub>2</sub> O, direct)	1.0–5.0 μm	Keck (NIRSPEC) IRTF (iShell)	Target brightness
Molecular abundance (H <sub>2</sub> O, inferred)	2500–3400 Å	Swift (UVOT)	Operational lifetime
Molecular abundances (CO, CS)	1400–3100 Å	HST (STIS, COS)	Oversubscription
Molecular abundances (H <sub>2</sub> O, CO <sub>2</sub> , CO)	Submillimeter	ALMA	February maintenance blackout
	Submillimeter	SMT	Monsoon season dead time
	MIR	JWST	ToO execution

measured with Keck-NIRSPEC or IRTF-iShell. The Stratospheric Observatory For Infrared Astronomy (Temi et al. 2018) could pursue similar objectives and measurements as JWST but with lessened sensitivity.

The detection of CO in 2I/Borisov is an excellent example of a limiting detection for an interstellar comet (Bodewits et al. 2020). When Borisov was detected at  $\sim 2$  au from both the Sun and the Earth, its *V*-band magnitude was  $\sim 17$ . The CO detection required 17,901 integration s (5 orbits of exposures) with the Hubble Space Telescope (HST) COS instrument at that magnitude. While the relationship between the *V*-band magnitude and CO production rates is not well understood, future UV spectral observations should be planned assuming similar requirements. Although space-based UV or IR observations are the most reliable way to characterize these parent molecules, they also require the objects to be brighter than for proxy measurements.

Proxies for H<sub>2</sub>O, like OH, OI, or atomic hydrogen, can be obtained for dim comets under fortuitous conditions. For comets of lower apparent brightness, near-ultraviolet (NUV), visible, and NIR observations will remain viable for a significant fraction of the observable trajectory. The OH radical can be converted to the H<sub>2</sub>O production rate (see Section 4 and references therein) and is observable from the ground in the NUV. However, these observations require telescopes with instrumentation sensitivity at wavelengths comparable to the atmospheric cutoff. Moreover, the extinction of 3100 Å light is extremely sensitive to airmass, so the comet’s sky position is as important as its brightness and H<sub>2</sub>O production rate. To circumvent this, the H<sub>2</sub>O production rate of Borisov was measured in the 0-0 band of OH emission with the Ultraviolet-Optical Telescope (UVOT) on the Swift Observatory (Xing et al. 2020). However, Swift is currently addressing a broken reaction wheel and is not available for observations. The OI emission also approximates the H<sub>2</sub>O production rate (McKay et al. 2020). This requires the oxygen emission to be sufficiently blue- or redshifted from atmospheric emission by the geocentric motion of the comet. This is only feasible for a subset of comets with suitable trajectories.

The carbon budget of an interstellar comet can be approximated by measuring the production rates of carbon-bearing radicals CN, C<sub>2</sub>, and C<sub>3</sub> between  $\sim 3800$  and  $\sim 5600$  Å. This is obtainable with visible-wavelength spectroscopy or specialized filters like the Hale–Bopp filter set (Farnham et al. 2000; which also encompasses an OH 0-0 transition). These specialized filter sets can be used to characterize faint comets not observable with visible spectroscopy. However, few specialized filter sets are available outside of the Lowell Observatory and NOIRLab telescope networks. The adoption of the Hale–Bopp or a similar filter set at more sites—especially very high altitude sites like Maunakea—would greatly increase our ability to characterize faint interstellar comets.

Characterizing daughter products will also permit classification of interstellar comets according to the solar system comet taxonomies (such as “typical” versus “depleted”; A’Hearn et al. 1995). Some comets exhibit apparently typical carbon budgets (Raymond et al. 2022) without easily detected emissions from these species (Schleicher 2008). The prevalence of this effect in interstellar comets will also contextualize them within the populations native to the solar system.

Generally, observations of carbon and oxygen atoms directly would require space-based ultraviolet observations, though exceptions do exist. The HST’s COS (Green et al. 2012) and STIS (Woodgate et al. 1998) instruments are the only currently available space-based ultraviolet-capable spectrographs sensitive to these emissions with guest observer capability.

### 7.3. Faint Interstellar Comets

The LSST will detect interstellar comets at or close to its limiting magnitude (Hoover et al. 2022). For these cases, some or all of the techniques outlined in the previous subsection cannot be applied. In this subsection, we highlight feasible alternative observational techniques when spectroscopic observations cannot be obtained.

The secular light curve, or brightness variations as a function of heliocentric distance, of a faint interstellar comet discovered

by a survey such as the LSST should still be straightforward to obtain. A reliable measure of its brightness will be automatically obtained every few days by the discovery survey. Larger telescopes will only be necessary when the comet is below the detection limits of the discovery survey. Outbound observations of comets have precedent, provide additional information about the evolution of activity, and contextualize the measurements obtained when the comets were brightest (such as Hale-Bopp; see Szabó et al. 2012).

The secular light curve of an interstellar comet will provide useful information regarding its composition. The light curve of inactive objects is driven only by the heliocentric distance and the phase angle. The brightness variations of active objects are dominated by dust lofted from the surface and fluorescence of gas molecules and radicals. These effects cause a steeper slope with respect to heliocentric distance as the active volatile ratios change (Biver et al. 1997). Brightness variations as an interstellar comet crosses various ice lines will provide some compositional constraints. For example, the extent to which the light curve is smooth or punctuated by large outbursts and periods of low activity at large heliocentric distances informs (i) which volatiles drive the activity and (ii) the compositional structure within the nucleus (Kareta et al. 2021). For comets that are bright and active enough to appear extended in imaging observations, the morphology of cometary comae can also provide constraints on the overall activity state and the volatiles driving the activity (Kim et al. 2020).

#### 7.4. Preparing for Observations of Future Interstellar Comets

In this subsection, we outline an observational strategy for a future interstellar comet with the primary goal of measuring the C/O ratio. The fraction of comets ejected from exterior to the CO snow line will be further constrained with every interstellar comet characterized in this manner. The LSST should detect  $\geq 10$  interstellar comets over 10 yr (Hoover et al. 2022),  $\sim 50\%$  of which have  $b < b_{21}$  (Figure 12), allowing for measurements of their C/O ratio. This will provide a statistical sample of  $\geq 7$  objects to constrain the fraction ejected that formed exterior to the CO snow line and yield insights into the efficiency of various scattering mechanisms.

The observations of Borisov serve as an example to build from for future interstellar comets. Multiple observations of H<sub>2</sub>O, CO<sub>2</sub>, and CO, as well as the typical cometary radicals OH, CN, and C<sub>2</sub>, were obtained and revealed the object's unique characteristics. Ideally, these observations will be repeated with future comets. Additionally, observations at heliocentric distances beyond 3 au pre- and postperihelion would inform the level to which ISM processing altered the surface composition. This would be vital information for estimating the primordial C/O ratio based on the measured one. Borisov was discovered  $\sim 3$  months prior to perihelion, limiting the time for preperihelion characterization of the molecular production rates. The drastic change in Borisov's H<sub>2</sub>O production rate postperihelion was explained by the removal of a CO-depleted and H<sub>2</sub>O-enriched surface (Bodewits et al. 2020). Preperihelion CO production rate measurements of a future interstellar comet would quantify the efficiency of this effect. Optimal observations of future interstellar comets would provide pre- and postperihelion characterization of the molecular abundances on either side of the H<sub>2</sub>O ice sublimation line at  $\sim 3$  au for the extent to which discovery and observing geometry allows. This corresponds to a minimum of 4 epochs

with detections or upper limits on H<sub>2</sub>O, CO<sub>2</sub>, and CO, as well as the more typical cometary radicals OH, CN, and C<sub>2</sub>.

The apparent magnitude of an interstellar comet is agnostic to the extended brightness of the coma. However, the activity level controls the brightness in exposures where the bandpass is sensitive to the fluorescence of the sublimating gas or reflected sunlight from lofted dust. The apparition of 21/Borisov was notably poor, partly because the comet only reached a geocentric distance of  $\sim 2$  au with a poor solar elongation angle. An LPC or JFC with the same absolute magnitude as Borisov would have been too poor of a target to propose observations for. However, due to its extrasolar origin, it was well characterized due to a global campaign. Therefore, limitations on the detectable activity level with certain telescopes for solar system comets should not be applied to interstellar comets.

The observatories capable of performing this suite of observations are presented in Table 4. The instrumentation and observatories are capable of measuring the C/O ratio of an interstellar comet independently. However, this system is susceptible to single-point failures. For example, in the event that the HST is unavailable during an interstellar comet apparition due to operational limitations, the H, C, O, and S atomic abundances cannot be measured directly with a single observation. If an interstellar comet is at a high decl. in the northern hemisphere during the monsoon season in Arizona and Swift UVOT is unavailable, it can only be characterizable by the IRTF and Keck observatories. This limits our ability to perform independent measurements of atomic, molecular, and radical abundances to ensure accuracy. Therefore, accurately measuring the C/O ratios of interstellar comets is directly linked to the stability of space-based observing platforms.

## 8. Conclusions

In this paper, we advocated for obtaining production rate measurements of the CO<sub>2</sub>, CO, and H<sub>2</sub>O of future interstellar comets. These measurements will provide lower limits on their primordial C/O ratios. In Section 2, we described how this ratio traces the formation location relative to the CO snow line. This technique is already used for extrasolar planets (Öberg et al. 2011). In Section 3, we reviewed the current measurements of stellar C/O ratios. Since the scatter in stellar C/O ratios is low, the C/O ratio of an interstellar comet is a reasonable tracer for formation location within a protostellar disk.

In Section 4, we reviewed measurements of the C/O ratio in solar system comets. We showed that measurements of CO<sub>2</sub>, CO, and H<sub>2</sub>O best approximate the C/O ratio, given their high abundance relative to other species. These measurements have revealed that most solar system comets formed interior to the CO snow line. Similar measurements of interstellar comets will constrain the fraction of ejected comets that formed exterior to the CO snow line. Objects 21/Borisov, C/2016 R2, and possibly 'Oumuamua likely formed in this region.

In Section 5, we quantified the relative importance of processing in the ISM and the solar system as a function of the lifetime and trajectory for an interstellar comet. We concluded that volatile production rates are unlikely to be representative of the primordial composition for most objects that will be detected with the LSST. Because of the preferential desorption of CO and CO<sub>2</sub> relative to H<sub>2</sub>O in the ISM, the measured C/O ratios are lower limits on the primordial one. In Section 6, we



show that the production rate ratios of  $Q(\text{CO})/Q(\text{H}_2\text{O}) < 0.2$  and  $Q(\text{CO})/Q(\text{H}_2\text{O}) > 1$  indicate formation interior and exterior to the CO snow line, respectively. It is possible that the primordial composition of an interstellar comet can be measured during a disintegration event, a tidal disruption event, or in situ during an impactor rendezvous mission. Additionally, measurements of the  $\text{H}_2\text{O}$  production rates of interstellar comets may encode information regarding the galactic star formation history (Lintott et al. 2022).

In Section 7, we reviewed the relevant observations of atoms, molecules, and radicals that constrain the C/O ratio of an interstellar comet. A range of space- and ground-based observatories covering the UV to submillimeter wavelengths will be required to measure abundances independently and characterize the composition accurately. Comprehensive atomic and molecular measurements would ideally be attempted on either side of the  $\text{H}_2\text{O}$  sublimation point ( $\sim 3$  au) prior to and postperihelion for a minimum of four observation epochs. We argued that compositional constraints can be obtained for faint interstellar comets that do not permit detailed spectroscopic characterization by monitoring for activity variation as a function of heliocentric distance via imaging campaigns.















Knowledge of the formation location of the population of ejected interstellar comets will yield key insights into the mechanisms driving planetary formation and evolution in exoplanetary systems and the solar system. If the population of interstellar comets mostly consists of objects that formed exterior to the CO snow line, then a natural interpretation is that the solar system also produced a population of CO-enriched comets that were ejected via early dynamical instability. It appears feasible that 2I/Borisov, and potentially R2 and 'Oumuamua, may be representative of this distinct class of comets. Moreover, the age of these interstellar comets could provide us with an estimate for the relative timing of the dynamical instabilities in exoplanetary systems. Based on theoretical modeling of the early timing of the instability in the solar system (Grav et al. 2011; Buie et al. 2015; Nesvorný et al. 2018; Clement et al. 2018, 2019; de Sousa et al. 2020; Nesvorný et al. 2021; Morgan et al. 2021) and the recent discovery of an excess of free-floating planets in the Upper Scorpius  $< 10$  Myr stellar association (Miret-Roig et al. 2022), it seems feasible that the majority of interstellar comets are ejected within the first  $< 10$  Myr of a planetary system's lifetime. If the majority of the population of interstellar comets formed interior to the CO snow line, this would imply that early giant planet migration is common in this region.

We thank Dave Jewitt, Konstantin Batygin, Jack Palmer, Juliette Becker, Kaitlin Kratter, Greg Laughlin, Fred Adams, and Robert Jedicke for useful conversations. We thank the scientific editor, Maria Womack, and the two anonymous reviewers for insightful comments and constructive suggestions that strengthened the scientific content of this manuscript.

A.D.F. acknowledges support from the National Science Foundation Graduate Research Fellowship Program under grant No. DGE-1746045. M.R.K. acknowledges support from the Australian Research Council through its Future Fellowships scheme, award FT180100375. L.A.R. gratefully acknowledges support from the Research Corporation for Science Advancement through a Cottrell Scholar Award. M.M. acknowledges support by NASA through NASA Hubble Fellowship grant

HST-HF2-51485.001-A awarded by the Space Telescope Science Institute. K.E.M. acknowledges support from NASA through Rosetta Data Analysis Program (RDAP) grant 80NSSC19K1306.

## ORCID iDs

Darryl Z. Seligman  <https://orcid.org/0000-0002-0726-6480>  
 Leslie A. Rogers  <https://orcid.org/0000-0003-0638-3455>  
 Samuel H. C. Cabot  <https://orcid.org/0000-0001-9749-6150>  
 John W. Noonan  <https://orcid.org/0000-0003-2152-6987>  
 Kathleen E. Mandt  <https://orcid.org/0000-0001-8397-3315>  
 Fred Ciesla  <https://orcid.org/0000-0002-0093-065X>  
 Adam McKay  <https://orcid.org/0000-0002-0622-2400>  
 Adina D. Feinstein  <https://orcid.org/0000-0002-9464-8101>  
 W. Garrett Levine  <https://orcid.org/0000-0002-1422-4430>  
 Jacob L. Bean  <https://orcid.org/0000-0003-4733-6532>  
 Mark R. Krumholz  <https://orcid.org/0000-0003-3893-854X>  
 Megan Mansfield  <https://orcid.org/0000-0003-4241-7413>  
 Devin J. Hoover  <https://orcid.org/0000-0002-7783-6397>  
 Eric Van Clepper  <https://orcid.org/0000-0002-5954-6302>

## References

- A'Hearn, M. F., Millis, R. C., Schleicher, D. O., Osip, D. J., & Birch, P. V. 1995, *Icar*, **118**, 223
- A'Hearn, M. F., Belton, M. J. S., Delamere, W. A., et al. 2011, *Sci*, **332**, 1396
- A'Hearn, M. F., Feaga, L. M., Keller, H. U., et al. 2012, *ApJ*, **758**, 29
- Almeida-Fernandes, F., & Rocha-Pinto, H. J. 2018, *MNRAS*, **480**, 4903
- Amarsi, A. M., Grevesse, N., Asplund, M., & Collet, R. 2021, *A&A*, **656**, A113
- Amarsi, A. M., Nissen, P. E., & Skúladóttir, Á 2019, *A&A*, **630**, A104
- Anderson, William Michael, J. 2010, PhD thesis, The Catholic Univ. of America
- Aravind, K., Ganesh, S., Venkataramani, K., et al. 2021, *MNRAS*, **502**, 3491
- Bagnulo, S., Cellino, A., Kolokolova, L., et al. 2021, *NatCo*, **12**, 1797
- Bailey, B. L., & Malhotra, R. 2009, *Icar*, **203**, 155
- Bannister, M. T., Schwamb, M. E., Fraser, W. C., et al. 2017, *ApJL*, **851**, L38
- Bannister, M. T., Opatom, C., Fitzsimmons, A., et al. 2020, arXiv:2001.11605
- Banzatti, A., Pinilla, P., Ricci, L., et al. 2015, *ApJL*, **815**, L15
- Bauer, J. M., Choi, Y.-J., Weissman, P. R., et al. 2008, *PASP*, **120**, 393
- Bauer, J. M., Stevenson, R., Kramer, E., et al. 2015, *ApJ*, **814**, 85
- Bedell, M., Bean, J. L., Meléndez, J., et al. 2018, *ApJ*, **865**, 68
- Belton, M. J. S., Hainaut, O. R., Meech, K. J., et al. 2018, *ApJL*, **856**, L21
- Bergman, P., Lerner, M. S., Olofsson, A. O. H., et al. 2022, *A&A*, **660**, A118
- Bertaux, J. L., Costa, J., Quémerais, E., et al. 1998, *P&SS*, **46**, 555
- Bialy, S., & Loeb, A. 2018, *ApJL*, **868**, L1
- Bieler, A., Altwegg, K., Balsiger, H., et al. 2015, *Natur*, **526**, 678
- Biver, N., & Bockelée-Morvan, D. 2016, *IAUFM*, **29A**, 228
- Biver, N., Bockelée-Morvan, D., Colom, P., et al. 1997, *Sci*, **275**, 1915
- Biver, N., Bockelée-Morvan, D., Crovisier, J., et al. 1999, *AJ*, **118**, 1850
- Biver, N., Bockelée-Morvan, D., Crovisier, J., et al. 2000, *AJ*, **120**, 1554
- Biver, N., Bockelée-Morvan, D., Crovisier, J., et al. 2006, *A&A*, **449**, 1255
- Bockelée-Morvan, D., & Biver, N. 2017, *RSPTA*, **375**, 20160252
- Bockelée-Morvan, D., Crovisier, J., Mumma, M. J., & Weaver, H. A. 2004, in Comets II, ed. M. Festou, H. U. Keller, & H. A. Weaver (Tucson, AZ: Univ. Arizona Press), 391
- Bodewits, D., Farnham, T. L., A'Hearn, M. F., et al. 2014, *ApJ*, **786**, 48
- Bodewits, D., Noonan, J. W., Feldman, P. D., et al. 2020, *NatAs*, **4**, 867
- Bönnhardt, H., Mumma, M. J., Villanueva, G. L., et al. 2008, *ApJL*, **683**, L71
- Bolin, B. T., Bodewits, D., Lisse, C. M., et al. 2020a, *ATel*, **13613**, 1
- Bolin, B. T., Weaver, H. A., Fernandez, Y. R., et al. 2018, *ApJL*, **852**, L2
- Bolin, B. T., Lisse, C. M., Kasliwal, M. M., et al. 2020b, *AJ*, **160**, 26
- Bond, J. C., O'Brien, D. P., & Lauretta, D. S. 2010, *ApJ*, **715**, 1050
- Bonev, B. P., Mumma, M. J., Gibb, E. L., et al. 2009, *ApJ*, **699**, 1563
- Brewer, J. M., Fischer, D. A., Valenti, J. A., & Piskunov, N. 2016, *ApJS*, **225**, 32
- Buie, M. W., Olkin, C. B., Merline, W. J., et al. 2015, *AJ*, **149**, 113
- Burrows, A., & Sharp, C. M. 1999, *ApJ*, **512**, 843
- Cameron, A. G. W. 1962, *Icar*, **1**, 13



- Castillo-Rogez, J., Landau, D., Chung, S.-J., & Meech, K. 2019, *Spaceflight Mechanics 2019* (San Diego, CA: American Astronautical Society), 2115, <https://authors.library.caltech.edu/100202/>
- Chambers, K. C., Magnier, E. A., Metcalfe, N., et al. 2016, arXiv:1612.05560
- Choi, Y. J., Weissman, P., Chesley, S., et al. 2006, *CBET*, 563, 1
- Cieza, L. A., Casassus, S., Tobin, J., et al. 2016, *Natur*, 535, 258
- Clement, M. S., Kaib, N. A., Raymond, S. N., Chambers, J. E., & Walsh, K. J. 2019, *Icar*, 321, 778
- Clement, M. S., Kaib, N. A., Raymond, S. N., & Walsh, K. J. 2018, *Icar*, 311, 340
- Cochran, A. L., & McKay, A. J. 2018, *ApJL*, 854, L10
- Cochran, A. L., & Schleicher, D. G. 1993, *Icar*, 105, 235
- Cochran, A. L., Levasseur-Regourd, A.-C., Cordiner, M., et al. 2015, *SSRv*, 197, 9
- Combi, M., Shou, Y., Fougere, N., et al. 2020, *Icar*, 335, 113421
- Cook, N. V., Ragozzine, D., Granvik, M., & Stephens, D. C. 2016, *ApJ*, 825, 51
- Cooper, J. F., Christian, E. R., Richardson, J. D., & Wang, C. 2003, *EM&P*, 92, 261
- Cordiner, M. A., Milam, S. N., Biver, N., et al. 2020, *NatAs*, 4, 861
- Cremonese, G., Fulle, M., Cambianica, P., et al. 2020, *ApJL*, 893, L12
- Crovisier, J., Biver, N., Bockelee-Morvan, D., et al. 1995, *Icar*, 115, 213
- Crovisier, J., Encrenaz, T., Lellouch, E., et al. 1999, in *ESA SP-427, The Universe as Seen by ISO*, ed. P. Cox & M. Kessler (Noordwijk: ESA), 161
- Ćuk, M. 2018, *ApJL*, 852, L15
- Dawson, R. I., & Johnson, J. A. 2018, *ARA&A*, 56, 175
- de la Fuente Marcos, C., & de la Fuente Marcos, R. 2020, *A&A*, 643, A18
- de Laplace, P. 1814, *Essai Philosophique sur les Probabilités* (Paris: Courcier)
- de Sousa, R. R., Morbidelli, A., Raymond, S. N., et al. 2020, *Icar*, 339, 113605
- Delgado Mena, E., Adibekyan, V., Santos, N. C., et al. 2021, *A&A*, 655, A99
- dello Russo, N., DiSanti, M. A., Magee-Sauer, K., Gibb, E., & Mumma, M. J. 2002, in *ESA SP-500, Asteroids, Comets, and Meteors: ACM 2002*, ed. B. Warmbein (Noordwijk: ESA), 689
- dello Russo, N., Kawakita, H., Vervack, R. J., & Weaver, H. A. 2016, *Icar*, 278, 301
- dello Russo, N., Mumma, M. J., DiSanti, M. A., et al. 2000, *Icar*, 143, 324
- dello Russo, N., Vervack, R. J., Weaver, H. A., et al. 2007, *Natur*, 448, 172
- Delsemme, A. H. 1973, *A&A*, 29, 377
- Desch, S. J., & Jackson, A. P. 2021, *JGRE*, 126, e2020JE006807
- Di Sisto, R. P., & Brunini, A. 2007, *Icar*, 190, 224
- Di Sisto, R. P., Fernández, J. A., & Brunini, A. 2009, *Icar*, 203, 140
- DiSanti, M. A., Anderson, W. M., Villanueva, G. L., et al. 2007, *ApJL*, 661, L101
- DiSanti, M. A., Bonev, B. P., Magee-Sauer, K., et al. 2006, *ApJ*, 650, 470
- Disanti, M. A., dello Russo, N., Magee-Sauer, K., et al. 2002, in *ESA SP-500, Asteroids, Comets, and Meteors: ACM 2002*, ed. B. Warmbein (Noordwijk: ESA), 571
- DiSanti, M. A., Mumma, M. J., Russo, N. D., & Magee-Sauer, K. 2001, *Icar*, 153, 361
- DiSanti, M. A., Villanueva, G. L., Milam, S. N., et al. 2009, *Icar*, 203, 589
- DiSanti, M. A., Bonev, B. P., Gibb, E. L., et al. 2016, *ApJ*, 820, 34
- DiSanti, M. A., Bonev, B. P., Russo, N. D., et al. 2017, *AJ*, 154, 246
- Do, A., Tucker, M. A., & Tonry, J. 2018, *ApJL*, 855, L10
- Domokos, G., Sipos, A. Á., Szabó, G. M., & Várkonyi, P. L. 2009, *ApJL*, 699, L13
- Domokos, G., Sipos, A. Á., Szabó, G. M., & Várkonyi, P. L. 2017, *RNAAS*, 1, 50
- Donitz, B. P., Castillo-Rogez, J. C., & Matousek, S. E. 2021, in *2021 IEEE Aerospace Conference (50100)* (Piscataway, NJ: IEEE), 1
- Drahus, M., Yang, B., Lis, D. C., & Jewitt, D. 2017, *MNRAS*, 468, 2897
- Drahus, M., Guzik, P., Udalski, A., et al. 2020, *ATel*, 13549, 1
- Duncan, M., Quinn, T., & Tremaine, S. 1988, *ApJL*, 328, L69
- Edgeworth, K. E. 1943, *JBAA*, 53, 181
- Edgeworth, K. E. 1949, *MNRAS*, 109, 600
- Engelhardt, T., Jedicke, R., Vereš, P., et al. 2017, *AJ*, 153, 133
- Enriquez, J. E., Siemion, A., Lazio, T. J. W., et al. 2018, *RNAAS*, 2, 9
- Everhart, E. 1972, *ApL*, 10, 131
- Faggi, S., Mumma, M. J., Villanueva, G. L., Paganini, L., & Lippi, M. 2019, *AJ*, 158, 254
- Farihi, J., Gänsicke, B. T., & Koester, D. 2013, *Sci*, 342, 218
- Farnham, T. L., Schleicher, D. G., & A'Hearn, M. F. 2000, *Icar*, 147, 180
- Feaga, L. M., A'Hearn, M. F., Sunshine, J. M., Groussin, O., & Farnham, T. L. 2007, *Icar*, 190, 345
- Feaga, L. M., A'Hearn, M. F., Farnham, T. L., et al. 2014, *AJ*, 147, 24
- Feldman, P. D., Festou, M. C., Tozzi, P., & Weaver, H. A. 1997, *ApJ*, 475, 829
- Feng, F., & Jones, H. R. A. 2018, *ApJL*, 852, L27
- Fernandez, J. A. 1980, *MNRAS*, 192, 481
- Fernández, J. A., Helal, M., & Gallardo, T. 2018, *P&SS*, 158, 6
- Fink, U. 2009, *Icar*, 201, 311
- Fitzsimmons, A., Snodgrass, C., Rozitis, B., et al. 2018, *NatAs*, 2, 133
- Fitzsimmons, A., Hainaut, O., Meech, K. J., et al. 2019, *ApJL*, 885, L9
- Flekkøy, E. G., Luu, J., & Toussaint, R. 2019, *ApJL*, 885, L41
- Fortney, J. J., Shabram, M., Showman, A. P., et al. 2010, *ApJ*, 709, 1396
- Francis, P. J. 2005, *ApJ*, 635, 1348
- Fraser, W. C., Pravec, P., Fitzsimmons, A., et al. 2018, *NatAs*, 2, 383
- Füglister, A., & Pfenniger, D. 2018, *A&A*, 613, A64
- Gaidos, E., Williams, J., & Kraus, A. 2017, *RNAAS*, 1, 13
- Gérard, E., Crovisier, J., Colom, P., et al. 1998, *P&SS*, 46, 569
- Gibb, E. L., Bonev, B. P., Villanueva, G., et al. 2012, *ApJ*, 750, 102
- Gibb, E. L., DiSanti, M. A., Magee-Sauer, K., et al. 2007, *Icar*, 188, 224
- Gomes, R. S., Morbidelli, A., & Levison, H. F. 2004, *Icar*, 170, 492
- Grav, T., Mainzer, A. K., Bauer, J., et al. 2011, *ApJ*, 742, 40
- Green, J. C., Froning, C. S., Osterman, S., et al. 2012, *ApJ*, 744, 60
- Grude Flekkøy, E., & Brodin, J. 2022, arXiv:2201.10327
- Gunnarsson, M., Bockelee-Morvan, D., Biver, N., Crovisier, J., & Rickman, H. 2008, *A&A*, 484, 537
- Guzik, P., & Drahus, M. 2021, *Natur*, 593, 375
- Guzik, P., Drahus, M., Rusek, K., et al. 2020, *NatAs*, 4, 53
- Hahn, G., & Bailey, M. E. 1990, *Natur*, 348, 132
- Hahn, J. M., & Malhotra, R. 1999, *AJ*, 117, 3041
- Hallatt, T., & Wiegert, P. 2020, *AJ*, 159, 147
- Hansen, B., & Zuckerman, B. 2017, *RNAAS*, 1, 55
- Harp, G. R., Richards, J., Jenniskens, P., Shostak, S., & Tarter, J. C. 2019, *AcAau*, 155, 51
- Harrington Pinto, O., Womack, M., Fernandez, Y., & Bauer, J. 2021, *AAS/DPS Meeting*, 53, 210.05
- Hayashi, C. 1981, *PTthPS*, 70, 35
- Heidarzadeh, T. 2008, in *Comets in the Laplacian Cosmos*, ed. T. Heidazadeh (Dordrecht: Springer), 187
- Hein, A. M., Perakis, N., Eubanks, T. M., et al. 2017, arXiv:1711.03155
- Herschel, W. 1812a, *RSPT*, 102, 115
- Herschel, W. 1812b, *RSPT*, 102, 229
- Hibberd, A., Hein, A., Eubanks, M., & Kennedy, R. I. 2022, arXiv:2201.04240
- Hibberd, A., Hein, A. M., & Eubanks, T. M. 2020, *AcAau*, 170, 136
- Hoang, M., Garnier, P., Gourlaouen, H., et al. 2019, *A&A*, 630, A33
- Hoang, M., Garnier, P., Lasue, J., et al. 2020, *A&A*, 638, A106
- Hoang, T., & Loeb, A. 2020, *ApJL*, 899, L23
- Hollenbach, D., Kaufman, M. J., Bergin, E. A., & Melnick, G. J. 2008, *ApJ*, 690, 1497
- Hoover, D. J., Seligman, D. Z., & Payne, M. J. 2022, *PSJ*, 3, 71
- Hsieh, C.-H., Laughlin, G., & Arce, H. G. 2021, *ApJ*, 917, 20
- Hui, M.-T., Ye, Q.-Z., Föhring, D., Hung, D., & Tholen, D. J. 2020, *AJ*, 160, 92
- Ivezić, Ž., Kahn, S. M., Tyson, J. A., et al. 2019, *ApJ*, 873, 111
- Jackson, A. P., & Desch, S. J. 2021, *JGRE*, 126, e2020JE006706
- Jackson, A. P., Tamayo, D., Hammond, N., Ali-Dib, M., & Rein, H. 2018, *MNRAS*, 478, L49
- Jaeger, M., Prosperi, E., Vollmann, W., et al. 2011, *IAUC*, 9213, 2
- James, N. D. 2018, *JBAA*, 128, 51
- Jewitt, D. 2003, *EM&P*, 92, 465
- Jewitt, D. 2009, *AJ*, 137, 4296
- Jewitt, D., Kim, Y., Mutchler, M., et al. 2020a, *ApJL*, 896, L39
- Jewitt, D., & Luu, J. 1993, *Natur*, 362, 730
- Jewitt, D., & Luu, J. 2019, *ApJL*, 886, L29
- Jewitt, D., Luu, J., Rajagopal, J., et al. 2017, *ApJL*, 850, L36
- Jewitt, D., Mutchler, M., Kim, Y., Weaver, H., & Hui, M.-T. 2020b, *ATel*, 13611, 1
- Jones, G. & ESA Comet Interceptor Team 2019, *Comet Interceptor A Mission to a Dynamically New Solar System Object*, [http://www.cometinterceptor.space/uploads/1/2/3/7/123778284/comet\\_interceptor\\_executive\\_summary.pdf](http://www.cometinterceptor.space/uploads/1/2/3/7/123778284/comet_interceptor_executive_summary.pdf)
- Jones, R. L., Chesley, S. R., Connolly, A. J., et al. 2009, *EM&P*, 105, 101
- Jones, R. L., Slater, C. T., Moeyens, J., et al. 2018, *Icar*, 303, 181
- Joss, P. C. 1973, *A&A*, 25, 271
- Kareta, T., Sharkey, B., Noonan, J., et al. 2019, *AJ*, 158, 255
- Kareta, T., Andrews, J., Noonan, J. W., et al. 2020, *ApJL*, 889, L38
- Kareta, T., Woodney, L. M., Schambeau, C., et al. 2021, *PSJ*, 2, 48
- Katz, J. I. 2018, *MNRAS*, 478, L95
- Kawakita, H., Dello, R. N., Vervack, R. J., et al. 2014, *ApJ*, 788, 110
- Kim, Y., Jewitt, D., Mutchler, M., et al. 2020, *ApJL*, 895, L34
- Knight, M. M., Protopapa, S., Kelley, M. S. P., et al. 2017, *ApJL*, 851, L31
- Kuiper, G. P. 1951, *PNAS*, 37, 1

- Laughlin, G., & Batygin, K. 2017, *RNAAS*, **1**, 43
- Laughlin, G., Bodenheimer, P., & Adams, F. C. 2004, *ApJL*, **612**, L73
- Lawler, M. E., & Brownlee, D. E. 1992, *Natur*, **359**, 810
- Lecacheux, A., Biver, N., Crovisier, J., et al. 2003, *A&A*, **402**, L55
- Leonard, F. C. 1930, *ASPL*, **1**, 121
- Levine, W. G., Cabot, S. H. C., Seligman, D., & Laughlin, G. 2021, *ApJ*, **922**, 39
- Levine, W. G., & Laughlin, G. 2021, *ApJ*, **912**, 3
- Levison, H. F., & Duncan, M. J. 1997, *Icar*, **127**, 13
- Levison, H. F., Morbidelli, A., Van Laerhoven, C., Gomes, R., & Tsiganis, K. 2008, *Icar*, **196**, 258
- Lin, H. W., Lee, C.-H., Gerdes, D. W., et al. 2020, *ApJL*, **889**, L30
- Lintott, C., Bannister, M. T., & Mackereth, J. T. 2022, *ApJL*, **924**, L1
- Lisse, C. M., Gladstone, G. R., Young, L. A., et al. 2022, *PSJ*, **3**, 112
- Luu, J. X., Flekkøy, E. G., & Toussaint, R. 2020, *ApJL*, **900**, L22
- Madhusudhan, N. 2012, *ApJ*, **758**, 36
- Magee-Sauer, K., Mumma, M. J., DiSanti, M. A., et al. 2008, *Icar*, **194**, 347
- Mamajek, E. 2017, *RNAAS*, **1**, 21
- Manzini, F., Oldani, V., Ochner, P., & Bedin, L. R. 2020, *MNRAS*, **495**, L92
- Mashchenko, S. 2019, *MNRAS*, **489**, 3003
- Masiero, J. 2017, arXiv:1710.09977
- McGlynn, T. A., & Chapman, R. D. 1989, *ApJL*, **346**, L105
- McKay, A. J., Cochran, A. L., Dello Russo, N., & DiSanti, M. A. 2020, *ApJL*, **889**, L10
- McKay, A. J., Cochran, A. L., DiSanti, M. A., et al. 2015, *Icar*, **250**, 504
- McKay, A. J., DiSanti, M. A., Kelley, M. S. P., et al. 2019, *AJ*, **158**, 128
- McKay, A. J., DiSanti, M. A., Cochran, A. L., et al. 2021, *PSJ*, **2**, 21
- McNeill, A., Trilling, D. E., & Mommert, M. 2018, *ApJL*, **857**, L1
- Meech, K., Castillo-Rogez, J., Hainaut, O., Lazio, J., & Raymond, S. 2019, *BAAS*, **51**, 552
- Meech, K., Castillo-Rogez, J., Bufanda, E., et al. 2021, *BAAS*, **53**, 282
- Meech, K. J., Weryk, R., Micheli, M., et al. 2017, *Natur*, **552**, 378
- Meltzer, B. 1949, *Natur*, **163**, 220
- Micheli, M., Farnocchia, D., Meech, K. J., et al. 2018, *Natur*, **559**, 223
- Miret-Roig, N., Bouy, H., Raymond, S. N., et al. 2022, *NatAs*, **6**, 89
- Moore, K., Castillo-Rogez, J., Meech, K. J., et al. 2021a, *BAAS*, **53**, 481
- Moore, K., Courville, S., Ferguson, S., et al. 2021b, *P&SS*, **197**, 105137
- Morbidelli, A., Levison, H. F., Tsiganis, K., & Gomes, R. 2005, *Natur*, **435**, 462
- Morgan, M., Seligman, D., & Batygin, K. 2021, *ApJL*, **917**, L8
- Moro-Martín, A. 2018, *ApJ*, **866**, 131
- Moro-Martín, A. 2019, *ApJL*, **872**, L32
- Moro-Martín, A. 2019, *AJ*, **157**, 86
- Moro-Martín, A., Turner, E. L., & Loeb, A. 2009, *ApJ*, **704**, 733
- Moses, J. I., Visscher, C., Fortney, J. J., et al. 2011, *ApJ*, **737**, 15
- Mousis, O., Aguichine, A., Bouquet, A., et al. 2022, *PSJ*, in press (arXiv:2103.01793)
- Mumma, M. J., DiSanti, M. A., Dello Russo, N., Magee-Sauer, K., & Rettig, T. W. 2000, *ApJL*, **531**, L155
- Mumma, M. J., McLean, I. S., DiSanti, M. A., et al. 2001a, *ApJ*, **546**, 1183
- Mumma, M. J., Dello Russo, N., DiSanti, M. A., et al. 2001b, *Sci*, **292**, 1334
- Mumma, M. J., DiSanti, M. A., Magee-Sauer, K., et al. 2005, *Sci*, **310**, 270
- Nesvorný, D., Roig, F. V., & Deienno, R. 2021, *AJ*, **161**, 50
- Nesvorný, D., Vokrouhlický, D., Bottke, W. F., & Levison, H. F. 2018, *NatAs*, **2**, 878
- Nesvorný, D., Vokrouhlický, D., Dones, L., et al. 2017, *ApJ*, **845**, 27
- Nissen, P. E. 2015, *A&A*, **579**, A52
- Öberg, K. I., Murray-Clay, R., & Bergin, E. A. 2011, *ApJL*, **743**, L16
- Oort, J. H. 1950, *BAN*, **11**, 91
- Ootsubo, T., Kawakita, H., Hamada, S., et al. 2012, *ApJ*, **752**, 15
- Opitom, C., Fitzsimmons, A., Jehin, E., et al. 2019, *A&A*, **631**, L8
- Paganini, L., Mumma, M. J., Villanueva, G. L., et al. 2012, *ApJL*, **748**, L13
- Paganini, L., Mumma, M. J., Boehnhardt, H., et al. 2013, *ApJ*, **766**, 100
- Paganini, L., DiSanti, M. A., Mumma, M. J., et al. 2014, *AJ*, **147**, 15
- Paganini, L., Mumma, M. J., Villanueva, G. L., et al. 2014, *ApJ*, **791**, 122
- Pau Sánchez, J., Morante, D., Hermosin, P., et al. 2022, *AcAau*, in press (arXiv:2107.12999)
- Phan, V. H. M., Hoang, T., & Loeb, A. 2021, arXiv:2109.04494
- Prialnik, D., Barucci, M. A., & Young, L. 2020, *The Trans-Neptunian Solar System* (Amsterdam: Elsevier)
- Price, E. M., Cleaves, L. I., Bodewits, D., & Öberg, K. I. 2021, arXiv:2103.12751
- Qi, C., Öberg, K. I., Wilner, D. J., et al. 2013, *Sci*, **341**, 630
- Quinn, T., Tremaine, S., & Duncan, M. 1990, *ApJ*, **355**, 667
- Radeva, Y. L., Mumma, M. J., Bonev, B. P., et al. 2010, *Icar*, **206**, 764
- Radeva, Y. L., Mumma, M. J., Villanueva, G. L., et al. 2013, *Icar*, **223**, 298
- Rafikov, R. R. 2018a, *ApJ*, **861**, 35
- Rafikov, R. R. 2018b, *ApJL*, **867**, L17
- Raymond, J. C., Giordano, S., Mancuso, S., Povich, M. S., & Bemporad, A. 2022, *ApJ*, **926**, 93
- Raymond, S. N., Armitage, P. J., & Veras, D. 2018, *ApJL*, **856**, L7
- Raymond, S. N., Kaib, N. A., Armitage, P. J., & Fortney, J. J. 2020, *ApJL*, **904**, L4
- Rickman, H. 2010, in *Dynamics of Small Solar System Bodies and Exoplanets*, Lecture Notes in Physics, Vol. 790, ed. J. Souchay & R. Dvorak (Berlin: Springer), 341
- Roth, N. X., Gibb, E. L., Bonev, B. P., et al. 2018, *AJ*, **156**, 251
- Roth, N. X., Gibb, E. L., Bonev, B. P., et al. 2020, *AJ*, **159**, 42
- Rubin, M., Altwegg, K., Balsiger, H., et al. 2019, *MNRAS*, **489**, 594
- Sarid, G., Volk, K., Steckloff, J. K., et al. 2019, *ApJL*, **883**, L25
- Schambeau, C. 2018, PhD thesis, Univ. of Central Florida
- Schleicher, D. G. 2008, *AJ*, **136**, 2204
- Seager, S., Richardson, L. J., Hansen, B. M. S., et al. 2005, *ApJ*, **632**, 1122
- Sekanina, Z. 1976, *Icar*, **27**, 123
- Sekanina, Z. 2019, arXiv:1901.08704
- Seligman, D., & Laughlin, G. 2018, *AJ*, **155**, 217
- Seligman, D., & Laughlin, G. 2020, *ApJL*, **896**, L8
- Seligman, D., Laughlin, G., & Batygin, K. 2019, *ApJL*, **876**, L26
- Seligman, D. Z., Kratter, K. M., Levine, W. G., & Jedicke, R. 2021a, *PSJ*, **2**, 234
- Seligman, D. Z., Levine, W. G., Cabot, S. H. C., Laughlin, G., & Meech, K. 2021b, *ApJ*, **920**, 28
- Senay, M. C., & Jewitt, D. 1994, *Natur*, **371**, 229
- Solontoi, M., Ivezić, Ž., & Jones, L. 2011, AAS Meeting, **217**, 252.11
- Szabó, G. M., Kiss, L. L., Pál, A., et al. 2012, *ApJ*, **761**, 8
- Tem, P., Hoffman, D., Ennico, K., & Le, J. 2018, *JAI*, **7**, 1840011
- Tingay, S. J., Kaplan, D. L., Lenc, E., et al. 2018, *ApJ*, **857**, 11
- Tiscareno, M. S., & Malhotra, R. 2003, *AJ*, **126**, 3122
- Trilling, D. E., Robinson, T., Roegge, A., et al. 2017, *ApJL*, **850**, L38
- Trilling, D. E., Mommert, M., Hora, J. L., et al. 2018, *AJ*, **156**, 261
- Tsiganis, K., Gomes, R., Morbidelli, A., & Levison, H. F. 2005, *Natur*, **435**, 459
- Vaghi, S. 1973, *A&A*, **24**, 41
- Vereš, P., & Chesley, S. R. 2017a, *AJ*, **154**, 13
- Vereš, P., & Chesley, S. R. 2017b, *AJ*, **154**, 12
- Veyette, M. J., Muirhead, P. S., Mann, A. W., & Allard, F. 2016, *ApJ*, **828**, 95
- Villanueva, G. L., Mumma, M. J., DiSanti, M. A., et al. 2011, *Icar*, **216**, 227
- Weaver, H. A., Feldman, P. D., A'Hearn, M. F., Dello Russo, N., & Stern, S. A. 2011, *ApJL*, **734**, L5
- Weaver, H. A., Feldman, P. D., McPhate, J. B., et al. 1994, *ApJ*, **422**, 374
- Weaver, H. A., Chin, G., Bockelée-Morvan, D., et al. 1999, *Icar*, **142**, 482
- Weidenschilling, S. J. 1977, *Ap&SS*, **51**, 153
- Whipple, F. L. 1964, *PNAS*, **51**, 711
- Wierzchos, K., & Womack, M. 2018, *AJ*, **156**, 34
- Wierzchos, K., & Womack, M. 2020, *AJ*, **159**, 136
- Wierzchos, K., Womack, M., & Sarid, G. 2017, *AJ*, **153**, 230
- Wilson, D. J., Gänsicke, B. T., Farihi, J., & Koester, D. 2016, *MNRAS*, **459**, 3282
- Wilson, D. J., Gänsicke, B. T., Koester, D., et al. 2015, *MNRAS*, **451**, 3237
- Womack, M., Sarid, G., & Wierzchos, K. 2017, *PASP*, **129**, 031001
- Womack, M., & Stern, S. A. 1997, *LPSC*, **28**, 1575
- Womack, M., & Stern, S. A. 1999, *SoSyR*, **33**, 187
- Woodgate, B., Kimble, R., Bowers, C., et al. 1998, *PASP*, **110**, 1183
- Xing, Z., Bodewits, D., Noonan, J., & Bannister, M. T. 2020, *ApJL*, **893**, L48
- Xu, S., Jura, M., Klein, B., Koester, D., & Zuckerman, B. 2013, *ApJ*, **766**, 132
- Xu, S., Jura, M., Koester, D., Klein, B., & Zuckerman, B. 2014, *ApJ*, **783**, 79
- Yang, B., Li, A., Cordiner, M. A., et al. 2021, *NatAs*, **5**, 586
- Ye, Q., Kelley, M. S. P., Bolin, B. T., et al. 2020, *AJ*, **159**, 77
- Ye, Q.-Z., Zhang, Q., Kelley, M. S. P., & Brown, P. G. 2017, *ApJL*, **851**, L5
- Zhang, Q., Ye, Q., & Kolokolova, L. 2020, *ATel*, **13618**, 1
- Zhang, Y., & Lin, D. N. C. 2020, *NatAs*, **4**, 852
- Zwart, P. S., Torres, S., Pelupessy, I., Bédorf, J., & Cai, M. X. 2018, *MNRAS*, **479**, L17